JOURNAL OF GEOPHYSICAL RESEARCH, VOL. 111, B07306, doi:10.1029/2005JB004180, 2006

# Rayleigh wave phase velocities, small-scale convection, and azimuthal anisotropy beneath southern California

Yingjie Yang[1,2] and Donald W. Forsyth[1]

Received 22 November 2005; revised 6 March 2006; accepted 14 April 2006; published 25 July 2006.

[1] We use Rayleigh waves to invert for shear velocities in the upper mantle beneath southern California. A one-dimensional shear velocity model reveals a pronounced low-velocity zone (LVZ) from 90 to 210 km. The pattern of velocity anomalies indicates that there is active small-scale convection in the asthenosphere and that the dominant form of convection is three-dimensional (3-D) lithospheric drips and asthenospheric upwellings, rather than 2-D sheets or slabs. Several of the features that we observe have been previously detected by body wave tomography: these anomalies have been interpreted as delaminated lithosphere and consequent upwelling of the asthenosphere beneath the eastern edge of the southern Sierra Nevada and Walker Lane region; sinking lithosphere beneath the southern Central Valley; upwelling beneath the Salton Trough; and downwelling beneath the Transverse Ranges. Our new observations provide better constraints on the lateral and vertical extent of these anomalies. In addition, we detect two previously undetected features: a high-velocity anomaly beneath the northern Peninsular Range and a low-velocity anomaly beneath the northeastern Mojave block. We also estimate the azimuthal anisotropy from Rayleigh wave data. The strength is ∼1.7% at periods shorter than 100 s and decreases to below 1% at longer periods. The fast direction is nearly E-W. The anisotropic layer is more than 300 km thick. The E-W fast directions in the lithosphere and sublithosphere mantle may be caused by distinct deformation mechanisms: pure shear in the lithosphere due to N-S tectonic shortening and simple shear in sublithosphere mantle due to mantle flow.

**Citation:** Yang, Y., and D. W. Forsyth (2006), Rayleigh wave phase velocities, small-scale convection, and azimuthal anisotropy beneath southern California, *J. Geophys. Res.*, *111*, B07306, doi:10.1029/2005JB004180.

## 1. Introduction

[2] Southern California lies astride the boundary between the Pacific plate and the North American plate. The complex evolution from a subduction boundary between the Farallon and North American plates to the present transform boundary [*Atwater*, 1998], involving rotating crustal blocks, passage of a triple junction, and opening of a slab window, has left scars in the lithospheric mantle and crust. That evolution continues today along with generation of new structural anomalies that can be detected with geophysical experiments. For example, the bend in the San Andreas fault introduces a component of compression generating the Transverse Range and the underlying, sinking tongue of the lower lithosphere that is revealed by high seismic velocities in the mantle [*Bird and Rosenstock*, 1984; *Humphreys and Hager*, 1990; *Kohler*, 1999]. A similar high-velocity anomaly beneath the Great (or Central) Valley is thought to be a sinking, lithospheric drip associated with delamination of the mantle lithosphere from beneath the volcanic fields of the southern Sierra Nevada [*Boyd et al.*, 2004; *Zandt et al.*, 2004]. Upwelling of hot asthenosphere to replace this delaminated lithosphere creates melting and low-velocity anomalies beneath the southern Sierra and adjacent Walker Lane [*Wernicke et al.*, 1996; *Boyd et al.*, 2004; *Park*, 2004]. Similarly, upwelling beneath zones of extension, like the Salton Trough, also induces low-velocity anomalies [*Raikes*, 1980]. The primary purpose of this paper is to improve the lateral and vertical resolution of these and other convective upwellings and downwellings by taking advantage of the nearly uniform areal coverage and sensitivity to asthenospheric and lithospheric structure provided by Rayleigh wave tomography.

[3] A number of investigations have been conducted to study the compressional wave velocity structure of the crust and upper mantle beneath southern California using P wave traveltime data [e.g., *Raikes*, 1980; *Humphreys and Clayton*, 1990; *Zhao and Kanamori*, 1992; *Zhao et al.*, 1996]. Surprisingly, there are few shear velocity or surface wave studies [e.g., *Press*, 1956; *Crough and Thompson*, 1977; *Wang and Teng*, 1994; *Polet and Kanamori*, 1997]. Because there were relatively few broadband stations, these early studies did not map lateral variations throughout southern California. The deployment of the TriNet seismic network, now incorporated in USArray, made it possible to perform three-dimensional (3-D) inversions for S wave velocity from surface wave data. In this study, we take finite

---

[1] Department of Geological Sciences, Brown University, Providence, Rhode Island, USA.

[2] Now at Center for Imaging the Earth's Interior, Department of Physics, University of Colorado, Boulder, Colorado, USA.

0148-0227/06/2005JB004180$09.00

frequency and scattering effects into account using a wide frequency range (0.007–0.04 Hz) and we use an array analysis method that employs many ray paths, thus improving the phase velocity resolution and resolving finer structure beneath southern California in a greater depth range.

[4] The second main goal of this investigation is to better resolve the origin of the seismic anisotropy observed in this region. Despite the complexity of lithospheric structure and tectonic history, the fast direction of shear wave splitting is nearly uniform throughout southern California. Shear wave splitting is often thought to be caused primarily by the anisotropy associated with lattice preferred orientation of olivine aligned by shearing flow in the mantle, with the fast direction roughly in the direction of mantle flow [*Silver*, 1996]. The near vertical propagation of SKS phases commonly used in splitting studies, however, yields very little resolution of the depth of the anisotropic layer. If the anisotropy is caused by the horizontal alignment of the olivine *a* axis, then the fast direction for splitting should coincide with the fast direction for Rayleigh wave propagation. The frequency dependence of the azimuthal anisotropy of Rayleigh waves should yield information on the vertical distribution of anisotropy, as waves of different periods are sensitive to different depth ranges.

[5] In southern California, the fast direction found in SKS splitting measurements is dominantly E-W [*Savage and Silver*, 1993; *Özalaybey and Savage*, 1995; *Liu et al.*, 1995; *Polet and Kanamori*, 2002]. There are debates, however, about the origin of the anisotropic structure in southern California, that is, whether the anisotropy is dominated by plate tectonism and/or by sublithospheric mantle flow. With a greater number of seismic sources and paths employed in this study, we can test whether there is a change in the fast direction or degree of anisotropy from lithosphere to asthenosphere and whether there is a shift in orientation between the Pacific and North American plates.

[6] In this paper, we use Rayleigh wave data recorded at TriNet/USArray network in southern California to invert for 2-D phase velocities and azimuthal anisotropy at periods ranging from 25 to 143 s. The 2-D phase velocities at different periods are then inverted for 3-D shear velocity structure. Finally, we compare the azimuthal anisotropy with shear wave splitting measurements from other studies to test models for the origin of the observed anisotropy.

## 2. Data Selection, Processing, and Station/Site Corrections

[7] We use fundamental mode Rayleigh waves recorded at 40 broadband seismic stations selected from the TriNet/USArray network in southern California (Figure 1). About 120 teleseismic events that occurred from 2000 to 2004 with surface wave magnitudes larger than 6.0 and epicentral distances from 30° to 120° were chosen as sources (Figure 2). The azimuthal coverage of these events is very good, which enables us to resolve both azimuthal anisotropy and lateral variations in phase velocity very well. The ray coverage for Rayleigh waves at the period of 50 s in the network region is shown in Figure 3. As expected from the distribution of the events, the coverage is excellent with many crossing rays both inside and outside the array. The ray density decreases somewhat with increasing period as fewer earthquakes generate waves with good signal-to-noise ratio at the longest periods. For example, the number of rays at period of 50 s is 3070, and it decreases to 2476 and 2292 at periods of 100 s and 143 s, respectively.

[8] We use vertical component Rayleigh wave seismograms, because they are not contaminated by Love wave interference and typically have lower noise levels than the horizontal components. The selected seismograms are filtered with a series of narrow band-pass (10 mHz), zero-phase shift, four-pole Butterworth filters centered at frequencies ranging from 7 to 40 mHz. All of the filtered seismograms are checked individually and only those with signal-to-noise amplitude ratio larger than 3 are selected, thus restricting the accepted frequency range separately for each event. If an event at a particular period is acceptable at some stations but not others, we check whether the low signal-to-noise ratio is caused by high noise or by destructive interference associated with multipathing or scattering along the path. If background noise levels are comparable to those at the acceptable stations, we retain the record because it will provide valuable information on the scattering pattern. Fundamental mode Rayleigh waves are isolated from other seismic phases by cutting the filtered seismograms using a boxcar window with a 50 s half cosine taper at each end. The width of the boxcar window is different for each period, but varies very little for different events at the same period and is identical for all seismograms from an individual source.

[9] To effectively use the focusing and defocusing of Rayleigh waves as constraints on the lateral variations in velocity structure, we need to carefully account for other influences on amplitude. These influences include: scattering and multipathing outside the array; local site response or amplification; instrument response, including erroneous responses; source radiation pattern; intrinsic attenuation and scattering from small-scale heterogeneities within the array; noise; and interference from other modes. We minimize the effects of noise by careful selection of the period range accepted for each station/event and by our application of frequency-dependent windowing. Windowing also effectively isolates the dispersed fundamental mode from higher modes, and the amplitude of the fundamental mode is usually much greater than that of higher modes for the shallow sources we employ. We neglect the source radiation pattern because the aperture of the array is small compared to the distance to the source; after eliminating events close to nodes in excitation of the surface waves, the expected variation in initial amplitude and phase with azimuth from the source is negligible. We correct for geometrical spreading on a sphere and model anelastic attenuation as part of the tomographic inversion. We assume amplitude decays with propagation distance x as $e^{-\gamma x}$, where $\gamma$ is the attenuation coefficient, and solve for the optimum value of $\gamma$ for each period. Since amplitude decay due to attenuation is relatively small within the study region, we only solve for an average attenuation coefficient at each period. Details of the resolution of attenuation are described in a separate paper [*Yang and Forsyth*, 2006]. The corrections for instrument responses and local site responses are discussed in the appendix. In section 3,

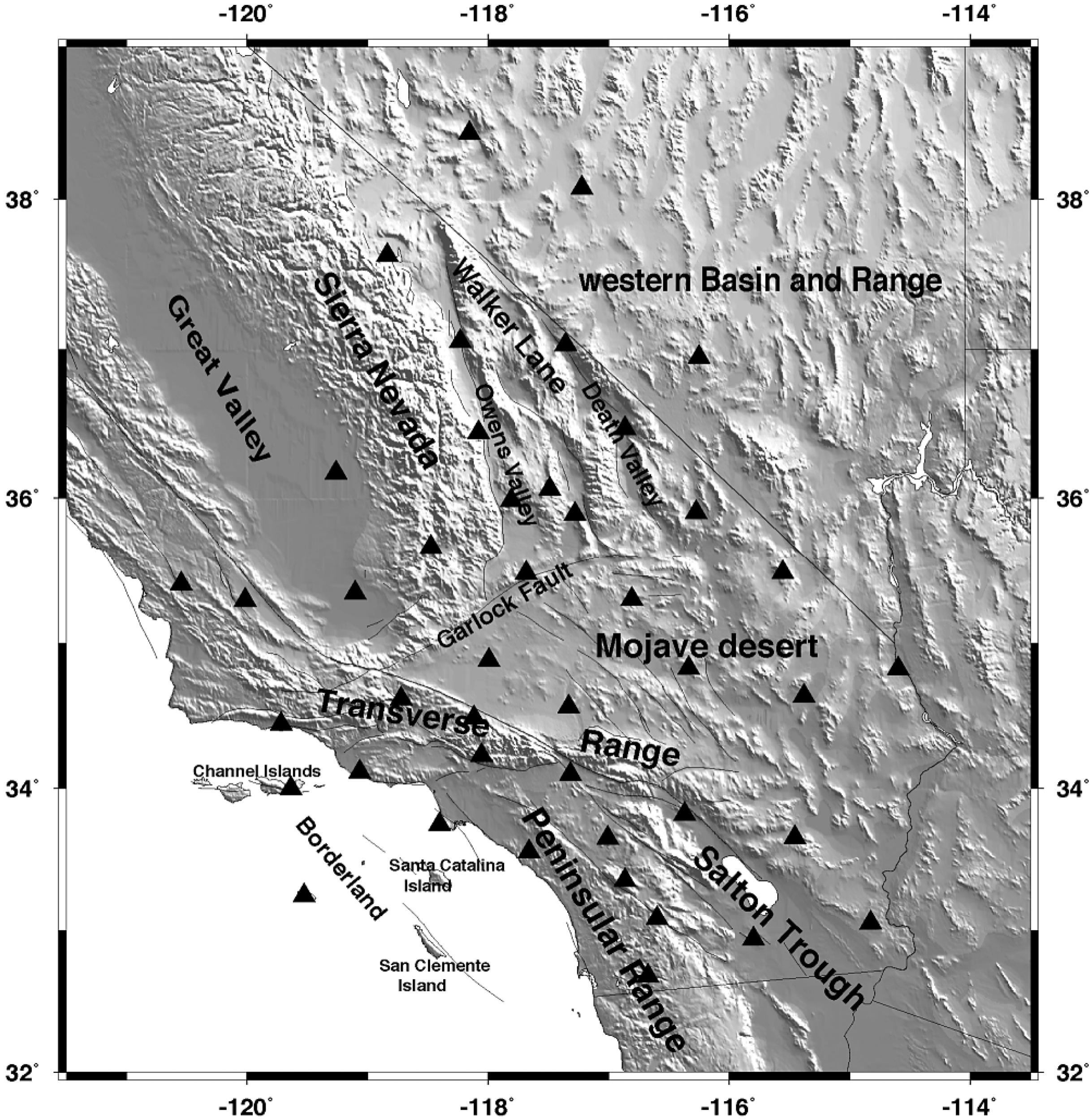

**Figure 1.** Topography of southern California. The locations of major tectonic provinces and faults (solid lines) are labeled. Triangles represent broadband three-component seismic stations used in this study.

we explain our approach to account for scattering and multipathing outside the array.

## 3. Methodology of Surface Wave Tomography

[10] One of the most important questions in phase velocity inversion of surface waves is how to represent incoming wavefields. The conventional approach is to regard incoming waves as plane waves propagating along great circle paths and use a two-station method to find the phase difference between two stations. However, most events show variations in amplitude or waveform across the array of a seismic network, which is indicative of scattering or multipathing caused by lateral heterogeneities between the source and the array. These effects will distort the incoming waves, causing deviations of incoming directions from the great circle azimuths and leading the wavefields to be nonplanar. Neglecting the nonplanar character can systematically bias the apparent phase velocities if only waveforms with constructive interference are selected [*Wielandt*, 1993]. In California, Rayleigh waves at short periods show strong interference due to scattering and multipathing. Seismograms of Rayleigh waves at long periods are simpler and clearer than at short periods due to the reduced complexity of seismic structures at depth and the intrinsically longer-wavelength averaging of surface waves.

[11] In this study, we use the sum of two plane waves, each with initially unknown amplitude, initial phase, and

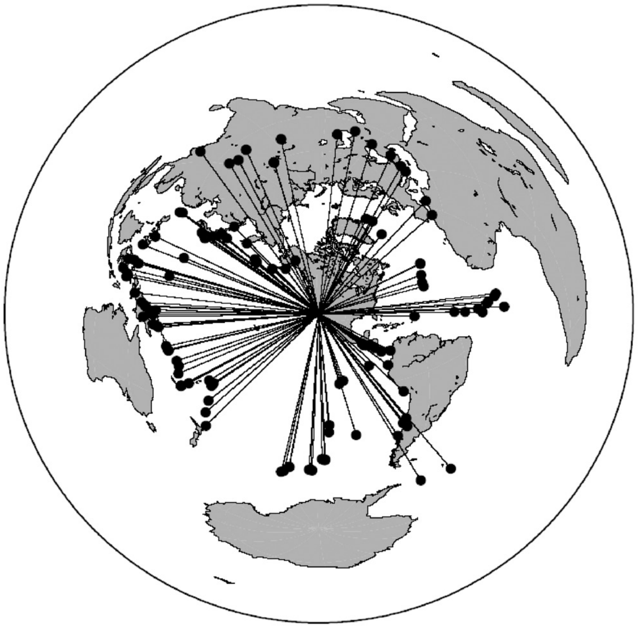

**Figure 2.** Azimuthal equidistant projection of earthquakes used in this study. The plot is centered on the center of the selected stations. The straight lines connecting each event to the array center represent the great circle ray paths. Note the good azimuthal coverage of the events.

propagation direction [*Forsyth et al.*, 1998; *Forsyth and Li*, 2005] to represent the nonplanar incoming wavefield, i.e., a total of six parameters to describe the incoming wavefield. This simple representation of the incoming wavefield has been successfully applied to other continental regions to obtain phase velocities and azimuthal anisotropy structures [*Li et al.*, 2003; *Weeraratne et al.*, 2003]. We recognize that the full complexity of the wavefield is not always well represented by this simple model, but this approach avoids the damping necessary for stability when a series of orthogonal polynomials, equivalent to many plane waves, is employed [*Friederich et al.*, 1994; *Friederich and Wielandt*, 1995; *Friederich*, 1998; *Pollitz*, 1999] and it provides a good approximation when the amplitude variation due to interference forms an approximately sinusoidal pattern elongated roughly in the direction of wave propagation, a common form. The wavefield parameters contain useful information about the incoming waves. In southern California, we find that Rayleigh waves coming from the Pacific Ocean are relatively simple with a primary wave propagating almost along the great circle path and a second wave that has very small amplitude. Incoming Rayleigh waves that have propagated across some complex structures, such as multiple ocean-continental boundaries or along island arcs, tend to have a significant second wave, and the propagation directions of both plane waves for these cases usually have larger deviations from the great circle path. In cases where the two-plane wave approximation is not a good model, the misfits are regarded as noise and that event for that particular period is automatically downweighted [*Forsyth and Li*, 2005].

[12] Another important issue is how to represent finite frequency effects, which are important in regional surface wave tomography since the goal typically is to resolve structures with scales on the order of a wavelength. *Yang and Forsyth* [2006] have shown that finite frequency scattering effects by heterogeneous structures can be accurately represented by the 2-D sensitivity kernels with the Born approximation derived by *Zhou et al.* [2004], even though near field terms are neglected in the vicinity of the receiver. Yang and Forsyth also demonstrated that employing the tomography method we use in this paper, utilizing the Born kernels in conjunction with the two-plane wave method, provides a much better resolution of local structure than is obtained representing the sensitivity kernels with a Gaussian-shaped influence zone [e.g., *Debayle and Sambridge*, 2004; *Sieminski et al.*, 2004; *Forsyth and Li*, 2005]. For each of the two plane waves, the 2-D sensitivity kernels at each period depend on reference phase velocity and the length and the shape of the window used to cut seismograms in data processing. An example of sensitivity kernels for a Rayleigh wave at period of 50 s windowed using a 300-s boxcar window is shown in Figure 4. Windowing the time series implicitly introduces frequency averaging into the Fourier analysis for the amplitude and phase of a particular frequency; the averaging creates interference that reduces the amplitude of the outer Fresnel zones. The kernels also have been smoothed with a 2-D Gaussian filter, because we interpolate velocities between nodal points using a 2-D Gaussian averaging function that restricts the scale of heterogeneities allowed. Perturbation of a nodal value perturbs the velocities in the surrounding region and our sensitivity function represents the integrated effect of that distributed disturbance. The filter for the example shown falls off to 1/e of its maximum value at a distance of 65 km from the center. The sensitivity kernels have a broad distribution and become broader with increas-

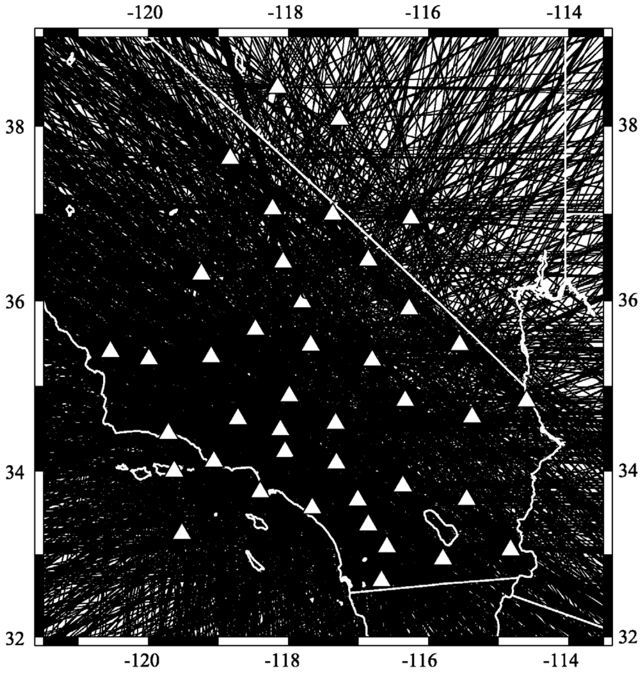

**Figure 3.** Great circle ray paths in southern California at a period of 50 s. White triangles represent stations, and white lines indicate state boundaries or coastlines. Note the dense crossing paths in the array area.

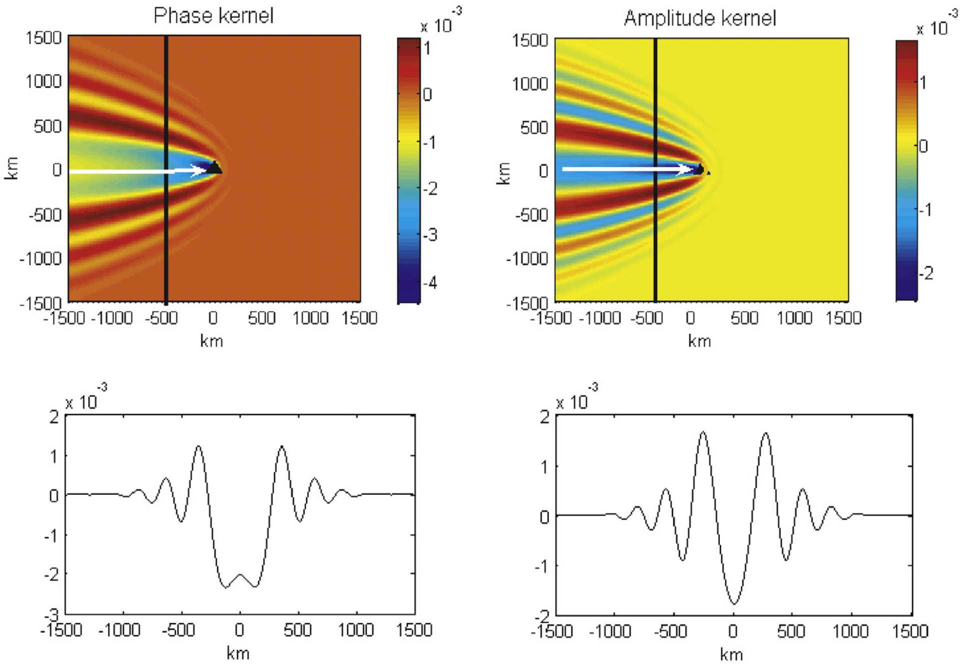

**Figure 4.** Two-dimensional sensitivity kernels for a 20 mHz plane Rayleigh wave. (top) Map views of kernels at surface. Black triangles denote receivers; white arrows indicate the incoming direction of the plane Rayleigh wave. (bottom) Cross section profiles of kernels along the bold lines marked in Figure 4 (top).

ing distance from the station along the ray path. The sensitivity is mainly concentrated in the region of the first two Fresnel zones, and quickly decreases in higher-order Fresnel zones.

[13] Surface wave phase velocity c in a uniform slightly anisotropic medium can be represented as

$$c(\omega,\psi) = A_0(\omega) + A_1(\omega)\cos(2\psi) + A_2(\omega)\sin(2\psi) + A_3(\omega)\cos(4\psi) + A_4\sin(4\psi), \quad (1)$$

where $\omega$ is frequency, $\psi$ is the azimuth of wave propagation, $A_0$ is the azimuthally averaged phase velocity, and $A_1$ to $A_4$ are azimuthal anisotropic coefficients [*Smith and Dahlen*, 1973]. We neglect the $A_3$ and $A_4$ terms here because they should be small for Rayleigh waves [*Smith and Dahlen*, 1973]. Scattering effects of the phase velocity perturbation $(c - c_o)$ relative to average phase velocities $c_o$ at each grid node are expressed as

$$\delta d = \iint_\Omega K_d^c(r,\omega)\left(\frac{c-c_o}{c_o}\right)dx^2, \quad (2)$$

where the integration is over the entire study region; $\delta d$ is shorthand for the phase delay or the relative amplitude variation with the corresponding phase kernel or amplitude kernel (Figure 4). The study region is parameterized with a total of 399 grid nodes that are distributed evenly in the study region. The density of grid nodes in the middle of the region is higher with 0.50° spacing in both longitude and latitude, and the density in the edge is lower with node spacing of 1.0°. The gridded region is much larger than the station-covered region, which is important since the outer region can absorb some variations of the wavefields that are more complex and cannot be completely represented by the interference of two plane waves.

[14] We use phase and amplitude data to simultaneously solve for the wavefield parameters of each event and the velocity parameters ($A_0$, $A_1$ and $A_2$) of each grid node in an iterative, least squares inversion. Each iteration involves two steps: first, we use a simulated annealing method to solve the six wavefield parameters for each event individually; second, we apply a generalized linear inversion [*Tarantola and Valette*, 1982] to find the phase velocity coefficients at each node, the station corrections, the attenuation coefficient, and changes to the wavefield parameters. We assigned an a priori error of 10% to the data in the first stage of inversion. After completing the inversion, we have estimates of the quality of fit for each individual event. We weight each event by the standard deviation of the residuals to deemphasize noisy data or complex wavefields that are not adequately represented by the two-plane wave approximation and then repeat the inversion to obtain the final result. Details of the inversion procedure are given by *Forsyth and Li* [2005] and *Yang and Forsyth* [2006].

## 4. Isotropic Phase Velocity Variations

[15] As required for any nonlinear inversion, we need an appropriate starting model for lateral phase velocity inversion. Thus, in the first step, we invert for average phase velocity by assuming that velocity is uniform in the entire study region at each period. The average dispersion curve is shown in Figure 5. The average phase velocities increase from 3.66 km/s at 25 s to 4.14 km/s at 143 s. The dense ray path coverage leads to small standard deviations for these

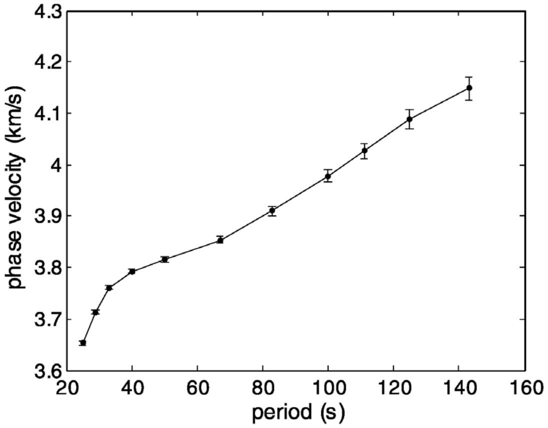

**Figure 5.** Average phase velocities for Rayleigh waves in southern California at 11 periods from 25 to 143 s. Error bars represent plus or minus two standard deviations from the mean.

averages, much smaller than reported in previous studies. There is a change in the slope of the dispersion curve around 33 s, indicating a change from sensitivity to the crust and uppermost mantle at short periods to primarily mantle sensitivity at longer periods. The concave upward shape of the dispersion curve from 50 to 80 s is an indicator of a possible low-velocity zone underlying a higher-velocity lithospheric lid.

[16] The 2-D lateral variations of phase velocities at each period are obtained using the average phase velocities as the starting model, allowing the phase velocity coefficients at each node to vary. The coefficients at these nodes are used to generate maps of lateral phase velocity variations on finer grids for plotting purposes (0.1° by 0.1°) by averaging the values at neighboring nodes using a Gaussian weighting function with a characteristic length, Lw, of 65 km, the same length used to smooth the 2-D sensitivity kernels described in section 3. The choice of the characteristic length has great effects on model resolution and variance. The usual tradeoff between model resolution and variance applies; the smaller Lw, the higher the resolution (i.e., smaller-scale variations of phase velocities can be resolved) and the larger the variance. We can also influence this tradeoff with our choice of a priori variances assigned to the nodal velocity parameters, which act as damping terms, but the imposed Gaussian averaging introduces a more uniform spatial scale to the smoothing than would be achieved by damping with a priori variances alone. We chose 65 km as the optimum value in this study after performing a number of experiments using different Lw. Standard errors of phase velocities in these maps are estimated from the modal covariance matrix of the phase velocity coefficients by linear error propagation [*Clifford*, 1975]. Figure 6h is a map of twice the standard errors of phase velocities at 50 s period, which can be interpreted as indicating how large the variations within the phase velocity map (Figure 6c) have to be to be significant at the approximate 95% confidence level. Standard errors are smallest at the center of the study area, where densities of both stations and crossing ray paths are greatest, and gradually increase toward the edge. Maps of phase velocities are masked using the 1% contour of twice standard errors for 50 s, eliminating the illustration of phase velocity variations in the region outside this contour that are relatively poorly constrained. Maps of standard errors at other periods are similar in form, but the magnitude of the errors increases with period, because at longer periods the Fresnel zone broadens, decreasing local sensitivity, the traveltime errors increase for the same relative phase error, and the number of seismograms with good signal-to-noise ratio decreases. At all the periods, the amplitude of anomalies we image are larger than two standard deviations. For instance, at the period of 100 s (Figure 6f), the amplitude of anomalies is typically 3%, while the average standard error is only ~0.6%.

[17] We have explored the dependence of the phase velocity anomalies on the starting model by using an alternative approach. Instead of using the average velocity at each period as the starting model, i.e., a laterally uniform starting model, we have tried starting with a laterally variable model consisting of the average velocity for a given period perturbed by the anomalies found for an adjacent period. We began at our best constrained period, 50 s, and worked progressively toward shorter and longer periods, each time using the percentage perturbations from the previous period as the starting model. In principle, this approach should lessen the effects of damping; assuming there is overlapping sensitivity to structure at adjacent periods and noise is uncorrelated, this procedure should allow the amplitude of true phase velocity perturbations to be more accurately mapped. We found, however, that with our choice of damping parameter and averaging length there was no significant difference in the models from those with uniform starting velocity; nowhere did the difference exceed about 1 standard deviation of the initial models.

[18] Figures 6a–6g are maps of phase velocities at periods of 25, 33, 50, 67, 83, 100, and 125 s. There are several pronounced features observed with patterns that vary gradually between adjacent periods. The continuity of features between adjacent periods is due to the overlapping depth ranges of Rayleigh wave sensitivity to structure. In contrast, the correlation between residuals to the models at these periods is very low, as reported also by *Weeraratne et al.* [2003], so artifacts due to noise or scattering from outside the array are unlikely to appear in more than one of these maps. Most of the anomalies we describe below have been previously detected in body or surface wave tomography studies.

[19] There is a striking low-velocity anomaly with north-south trend imaged in the region of the southeastern Sierra Nevada and Walker Lane volcanic fields from 25 to 50 s. Strong high velocity anomalies are observed in the offshore Borderland region at 25 to 33 s and in the Transverse Range from 33 s up to 83 s. High velocities are also imaged in the southern Central Valley at periods shorter than 67 s and in the Peninsular Range near the California/Mexico border at periods longer than 50 s. The Peninsular Range anomaly has not been reported previously, perhaps due to the scarcity of stations and the greater apparent depth (as it is strongest at the longest periods). There is a small low-velocity anomaly in the Salton Trough, also detected in many previous P wave studies, that is present at all periods, with its center shifting to the southeast with

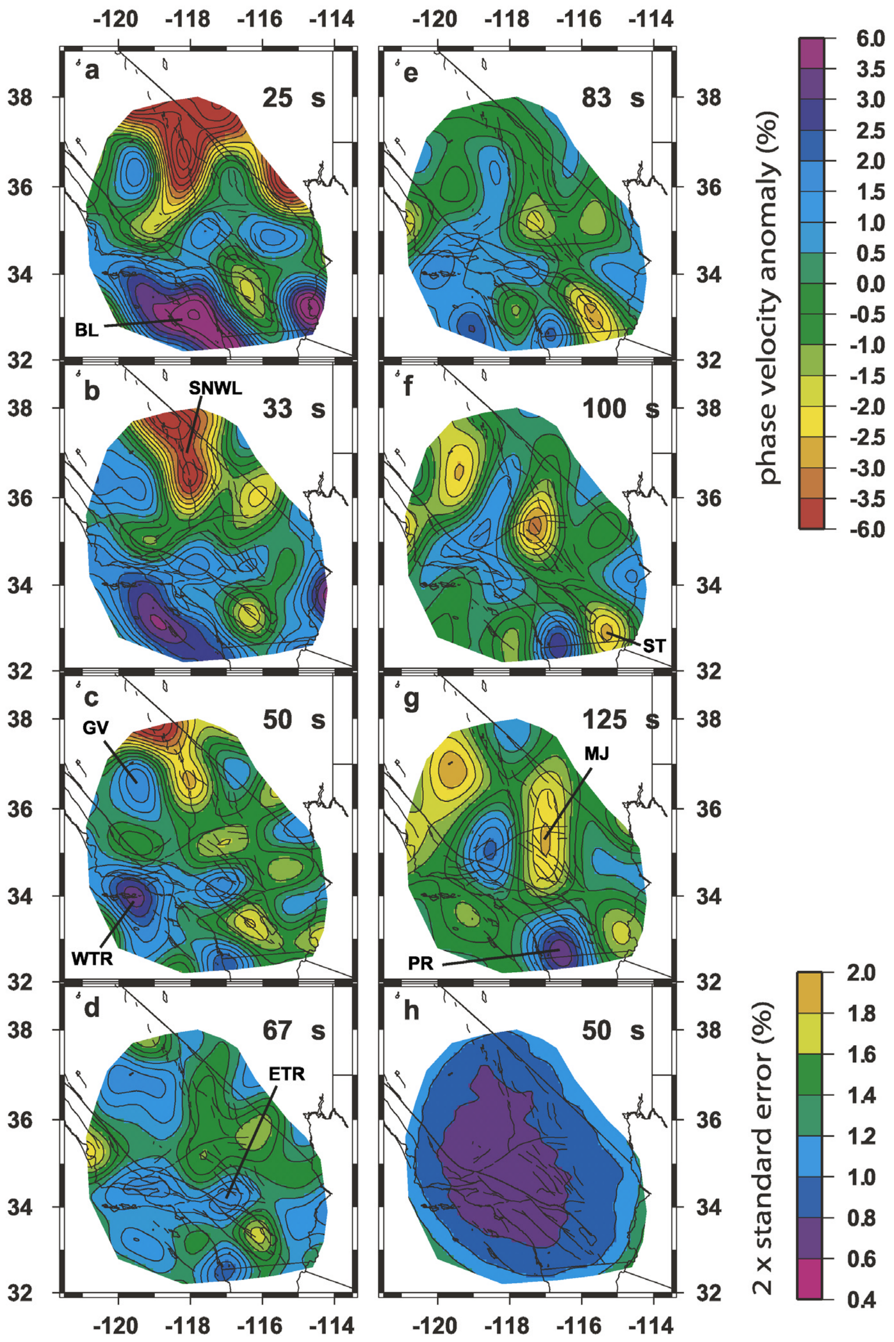

**Figure 6.** Maps of Rayleigh wave phase velocity anomalies and phase velocity uncertainties. The phase velocity maps are shown at seven periods: (a) 25 s, (b) 33 s, (c) 50 s, (d) 67 s, (e) 83 s, (f) 100 s, and (g) 125 s. Velocity anomalies are calculated relative to the average phase velocities of southern California shown in Figure 8. (h) Map of two times the standard errors of the phase velocities at 50 s. The phase velocity maps are masked using the approximate 1.2% error contour at period of 50 s. Anomalies discussed in the text are labeled: BL, Borderlands; SNWL, Sierra Nevada, Walker Lane; GV, Great Valley; WTR, Western Transverse Range; ETR, Eastern Transverse Range; MJ, Mojave; and PR, Peninsular Range.

increasing period. The low-velocity anomaly at periods equal to or greater than 83 s centered at 35.3°N, 117.2°W in the northern Mojave desert has not previously been reported, again, perhaps due to its greater apparent depth. Some small-scale anomalies are observed usually at the edges of the maps at individual periods, which we consider to be questionable features due to poor resolution in these marginal areas.

## 5. Average Shear Wave Velocity Structure

[20] Phase velocities can only tell us integrated information about the upper mantle. In order to obtain direct

information at various depths that can be interpreted in terms of temperature anomalies, the presence of melt or dissolved water, etc., we invert phase velocities for shear wave velocities. Rayleigh wave phase velocities primarily depend on S wave velocities, less on density and P wave velocities. P wave sensitivity is confined primarily to the crust. Therefore we only solve for S wave velocities by coupling P wave velocities to S wave velocities using a constant Poisson's ratio, which is a reasonable approximation for the materials of the crust and uppermost mantle. Deeper in the mantle, Poisson's ratio is probably not constant, but at those depths, the sensitivity to P wave velocity is negligible.

[21] The data in this inversion are phase velocities of the 11 periods from 25 to 143 s at each point of the phase velocity maps. We perform a series of 1-D inversions at each map point to build up a 3-D model. The model parameters are shear wave velocities in each of ∼20-km-thick layers extending from the surface to 200 km with structure below that depth fixed to the starting model. Synthetic phase velocities and partial derivatives of phase velocities with respect to the change in P and S wave velocities in each layer are computed using Saito's algorithm [*Saito*, 1988]. The model parameters are slightly damped by assigning prior standard deviations of 0.2 km/s in the diagonal terms of model covariance matrix and smoothed by adding off-diagonal terms to the model covariance matrix that enforce a 0.3 correlation in changes of shear velocities in the adjacent layers.

[22] Because the inversion is somewhat nonlinear and highly underdetermined due to the limitations of surface wave vertical resolution, details of the resultant model on scales smaller than the resolving length will depend strongly on the starting model and relative damping for shear wave velocities and the crustal thickness. In order to obtain an appropriate reference model in our study region, we first perform an inversion using the average phase velocities for the entire region (Figure 5) with the TNA model of *Grand and Helmberger* [1984] (Figure 7) as the starting model. The TNA model represents the average upper mantle shear structure in western United States. The crustal thickness is fixed at 30 km, which is the average crustal thickness in southern California constrained from receiver function studies [*Zhu and Kanamori*, 2000; *Magistrale et al.*, 2000]. For this reference model, velocity is allowed to vary to a depth of 400 km, because the standard deviations of the average phase velocities are much smaller than the uncertainties associated with lateral variations, yielding better depth resolution.

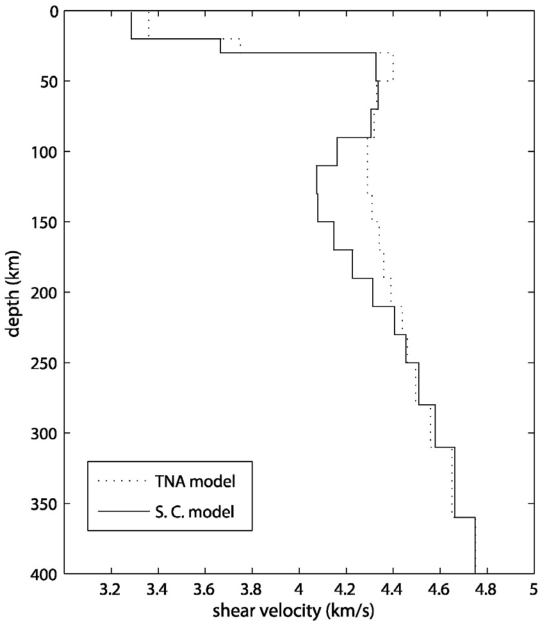

**Figure 7.** Average shear velocity structure beneath southern California (solid line). This model is inverted from the dispersion curve shown in Figure 5 using model TNA [*Grand and Helmberger*, 1984], dashed line, as a starting model.

[23] The final 1-D reference model is shown in Figure 7. The most striking feature is a low-velocity zone from 90 to 210 km with the lowest velocity of 4.05 to 4.1 km/s at a depth of 125 km, which is consistent with the low shear velocities in the upper mantle observed by *Polet and Kanamori* [1997]. Beneath 230 km, the S wave velocity is indistinguishable from the TNA model. This low-velocity zone underlies a relatively high velocity upper mantle lid. The velocity contrast between the low-velocity zone and the upper mantle lid is about 6%. If we adopt the depth of maximum negative velocity gradient as the best estimate of the base of lithosphere, which is the most frequently used criterion in surface wave studies of both oceanic and continental regions, our best estimate of average lithospheric thickness in southern California is about 90 km. Some other studies also observed similar thickness of the lithosphere in this area. For example, based on the depth extent of the P wave velocity contrast between the Salton Trough and surroundings [*Humphreys and Clayton*, 1990], *Humphreys and Hager* [1990] estimated lithospheric thickness of about 70–100 km. The surface wave study by *Wang and Teng* [1994] showed that the lithospheric thickness in the Mojave Desert is about 100 km. The differences between these studies is reasonable considering the uncertainties of about 20 km in the depth to the maximum gradient with resolving lengths of about 50 km at 90 km.

[24] The combination of a 90-km-thick lithosphere and average shear velocity of only about 4.35 km/s in this high velocity mantle lid suggests that composition or phase state may control the thickness of the lid and the existence of the pronounced low-velocity zone, rather than the temperature structure alone. One contributing factor to a low average velocity in the lid is the inclusion of a region within the average in which the lithosphere is completely removed (see later discussion of lateral variations), but much of southern California lies within 2% of the average. In other areas of comparable lid thickness, such as old oceanic lithosphere [*Nishimura and Forsyth*, 1989] or eastern North America [*van der Lee*, 2002; *Li et al.*, 2003; *Rychert et al.*, 2005], Rayleigh wave inversions yield typical lithosphere S velocities of 4.6 to 4.7 km/s. A ∼0.30 km/s or 6.5% decrease in velocity of the lid compared to these other areas requires an increase in temperature of ∼750°C if accomplished purely through elastic effects [*Stixrude and Lithgow-Bertelloni*, 2005]. The effects of anelasticity can greatly enhance the temperature sensitivity; using the model of *Jackson et al.*

[2002], anelasticity reduces the temperature change required to a minimum of about 200–250°C. Attributing the velocity reduction to anelastic effects, however, requires high attenuation and, equivalently, low seismic quality factor Q. We find Q for the shear modulus in the high velocity lid in southern California to be on the order of 200 [*Yang and Forsyth*, 2006], much too high to have a major effect on apparent velocity. Thus the average temperature contrast between the southern California lid and the lithosphere in stable continental regions is likely to significantly exceed 250°C. On the basis of heat flow, *Humphreys and Hager* [1990] estimated temperature at the base of a 30-km-thick crust in southern California to be ~800°C, in contrast to typical values of 500–550°C at the base of 40-km-thick Proterozoic continental crust [*Rudnick et al.*, 1998].

[25] If the lithosphere is a thermal boundary layer and the mantle from 30 to 90 km is several hundred degrees hotter than the lithosphere in eastern North America, why is the high velocity lid nearly the same thickness and why is there a large velocity drop into the low-velocity zone? Under ordinary circumstances, the thermal boundary layer would be expected to thin as the average temperature in a given depth range increases and the transition at the base of the thermal boundary layer should be gradual with no further drop in velocity beneath it. One possibility is that the thickness is controlled by a compositional or state change, such as the presence of water or melt in the low-velocity zone with the base of the high-velocity lid representing a dehydration boundary or the solidus. Indeed, many estimates of lithospheric thickness have presumed that the base of the lithosphere is the solidus [e.g., *Humphreys and Hager*, 1990]. Another possibility discussed by Humphreys and Hager is that there is a nonsteady state temperature profile in the lithosphere with a large warming gradient at its base due to cooling of the lower continental lithosphere during the time of subduction of the Farallon slab, now replaced by asthenosphere. It is difficult to explain, however, shear velocities as low as 4.1 km/s in the mantle without the existence of melt [*Stixrude and Lithgow-Bertelloni*, 2005] or a solid-state mechanism that leads to much higher attenuation than we observe [*Faul and Jackson*, 2005].

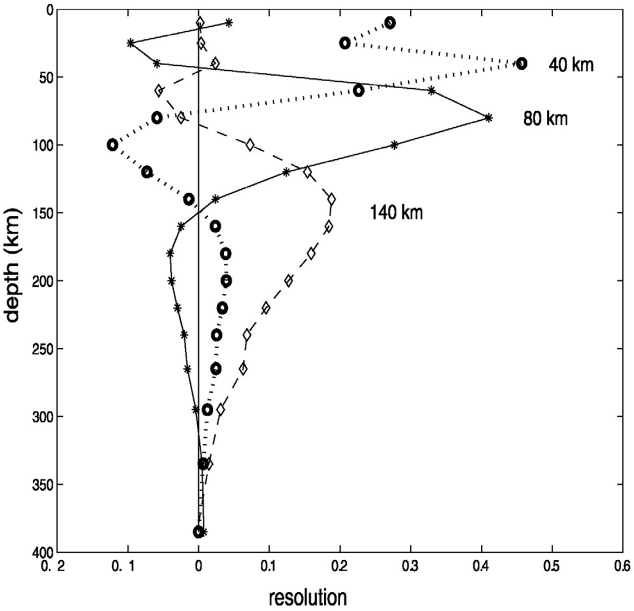

**Figure 8.** Resolution kernels of shear velocity inversion for the reference model at depths of 40 km (circles and dotted line), 80 km (stars and solid line), and 140 km (diamonds and dashed line).

[26] As in any inversion problem, we need to evaluate the resolution of model parameters, which can tell us how well shear velocities at different depths are resolved. The elements of the resolution matrix that can be computed in the inversion provide useful measurements of resolution. The rank of the resolution matrix provides an overall measurement of resolution, which describes the number of pieces of independent information about the model parameters provided by the data, i.e., the number of linearly independent combinations of model parameters that can be resolved. For the average shear velocity of the entire region, the rank is 4.2. For typical points in Figure 6, the rank is 3.0. The rank for the entire region is higher than for a typical point, because the uncertainties of average phase velocities for the whole region are much smaller than for a typical point. If the resolution matrix is an identity matrix, each of the model parameters is perfectly resolved and the solution is equal to the true solution. If the row vector of the resolution matrix has nonzero off-diagonal terms that spread about the diagonal term, the particular solution will represent a smoothed solution over a range of depths. The resolution length is a measurement of this depth range over which the average shear velocity can be well resolved, i.e., the sum of the diagonal elements of the resolution matrix over that length scale sums to one piece of information and the resolution kernel is reasonably compact. For example, at the depth of 50 km, the resolution length is ~40 km. The resolution kernels at three depths for the average model are plotted in Figure 8, which shows how the information about shear velocity at a particular depth is entwined with the information about shear velocities in adjacent layers. The resolution length increases with depth, because longer-period Rayleigh waves sensitive to deeper structures have broader sensitivity ranges. Resolution kernels for the point-by-point inversions are similar in the upper 150 km with the primary loss of information compared to the average model coming at depths greater than 200 km. Below 200 km, there is little information available from phase velocity data about lateral variations in structure, so we fix the models to the reference model in inverting for the 3-D velocity structure.

## 6. Crustal Structure

[27] Combining all the inversion results of shear wave velocities beneath each point, we form a model of the 3-D shear velocity structures in southern California. Rayleigh waves cannot directly detect seismic discontinuities since they are sensitive to the seismic velocity structure over a broad depth range; there is a large tradeoff between the crustal thickness and the seismic velocities of lower crust and uppermost mantle. For instance, a 5-km change of Moho depth with a 0.7 km/s shear velocity contrast across the Moho can be approximately matched with a 0.1 km/s velocity change over a depth range of 20 to 55 km in the inversion. In order to constrain the tradeoff between them,

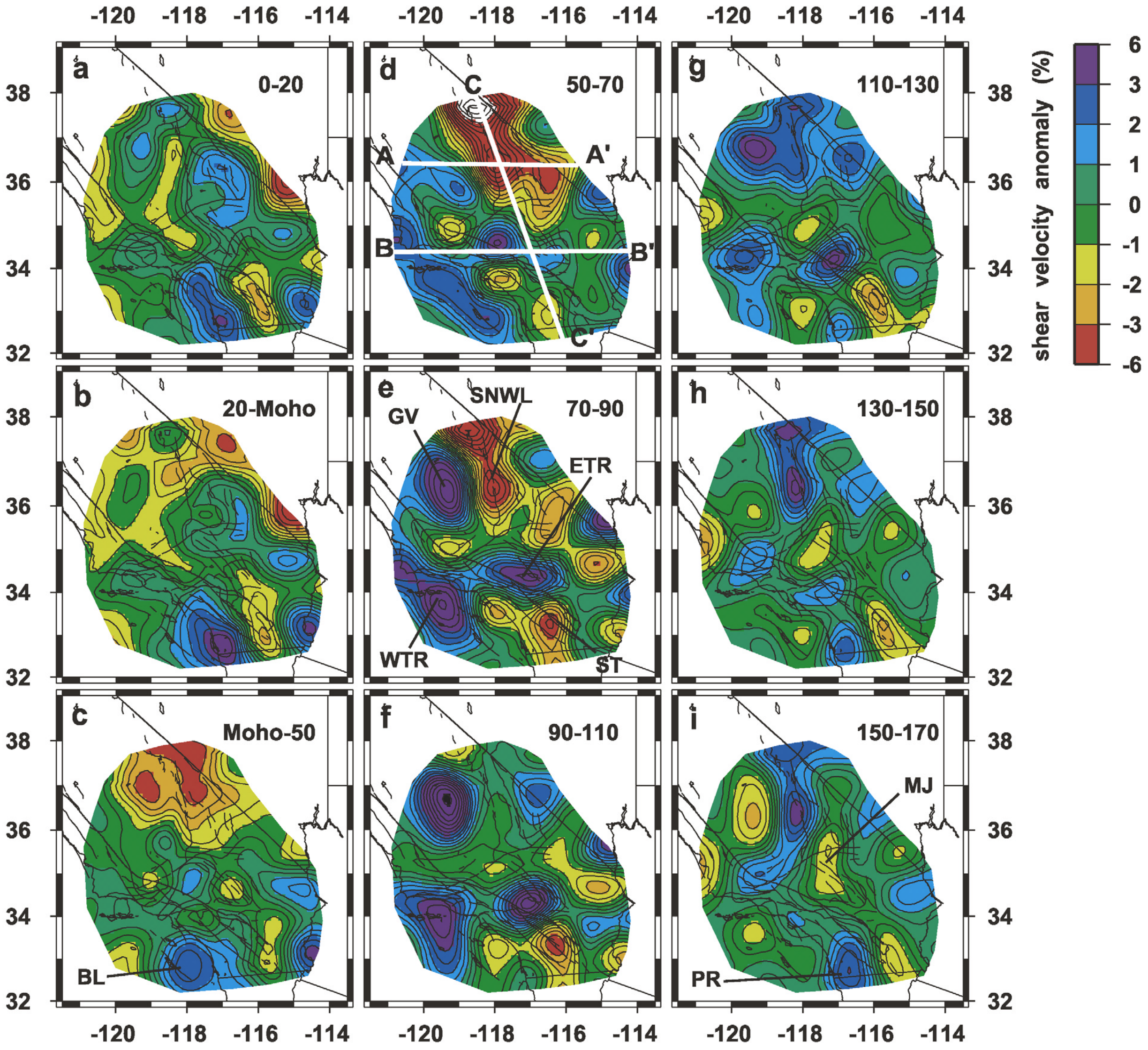

**Figure 9.** Maps of shear wave velocity anomalies in nine layers from the surface to a depth of 170 km. The velocity anomalies are relative to the 1-D reference model shown in Figure 7 (solid line). The white bold lines in Figure 9d are locations of vertical cross sections shown in Figure 10. Major shear wave velocity anomalies are labeled as the southern Sierra Nevada and Walker Lane anomaly (SNWL), the Great Valley anomaly (GV), the eastern Transverse Range anomaly (ETR), the western Transverse Range anomaly (WTR), the Borderlands anomaly (BL), the Salton Trough anomaly (ST), the Mojave anomaly (MJ), and the Peninsular Range anomaly (PR).

we use prior information of crustal thickness from other studies and restrict the change of crustal thickness within a small range from the starting values by assigning an a priori model standard deviation of 2 km to the crustal thickness. *Zhu and Kanamori* [2000] estimated the crustal thickness and *Vp*/*Vs* under a large number of three-component seismic stations using a receiver function stacking technique. The calculated Moho depth is 29 km on average and varies from 21 to 37 km. We use this model to set starting values for crustal thickness in the tomographic images illustrated in Figure 9.

[28] In the crust, the most pronounced feature is a high velocity anomaly along the southern Peninsular Ranges (Figures 9a and 9b), which is consistent with fast P wave velocities reported for the lower crust [*Zhao and Kanamori*, 1992; *Zhao et al.*, 1996] or even thinner crust than estimated by Zhu and Kanamori. A slightly high anomaly is observed in the Death Valley region. In the Salton Trough region, the velocity is low. Strong anomalies are also imaged in the crust along the eastern edge of our study area: a high velocity anomaly along the southern Arizona/California border and a low-velocity anomaly in southern Nevada. We regard these edge anomalies as questionable. As more stations are deployed in USArray in Arizona and Nevada, we should be able to resolve their strength and shape with more confidence.

[29] Our resolved map of crustal thickness differs little from the interpolated starting model of Zhu and Kanamori since we assign strong damping to the crustal thickness parameter. Some of the lower crustal and uppermost mantle

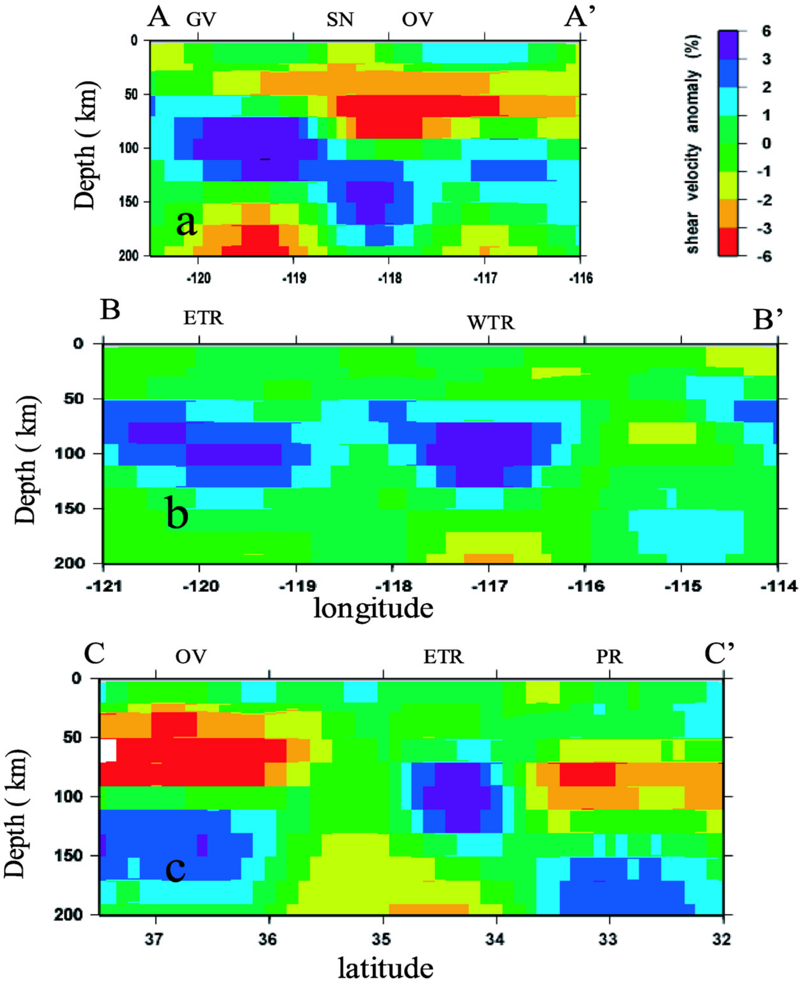

**Figure 10.** Vertical cross sections of shear wave velocity structures. The locations of the three profiles are delineated in Figure 9d. Abbreviations for major tectonic units are labeled on the top of cross sections as the Great Valley (GV), the Sierra Nevada (SN), the Owens Valley (OV), the eastern Transverse Range (ETR), the western Transverse Range (WTR), and the Peninsular Range (PR).

anomalies probably represent errors in crustal thickness. As discussed below, we think the crustal thickness in much of the California Borderlands region in the model is overestimated, because the model has simply interpolated between stations in the Peninsular Range and the few island stations off the coast where receiver function analyses are available. A better model of crustal thickness could be created by combining the seismological information with other geologic and tectonic indicators, but we can use the apparent velocity anomalies to indicate places where the crustal model is likely to be in error. Our focus is on upper mantle anomalies, but we have to be cautious in interpreting anomalies in the shallowest mantle, because there are possible trade-offs where crustal thickness is poorly constrained by other observations.

## 7. Upper Mantle Anomalies and Small-Scale Convection

### 7.1. Delamination Beneath the Sierra Nevada

[30] In the uppermost mantle, strong low-velocity anomalies exist underneath the eastern edge of the southern Sierra Nevada and the Walker Lane region from the Moho to 90 km underlain by high velocities at depths greater than 110 km (Figures 9c–9e, 10a, and 10c). The anomaly in the 50- to 70-km depth range reaches an amplitude of 5–6%, which is equivalent to the contrast between the high velocity lid and the low-velocity zone, indicating a complete absence of the lithosphere at depths greater than 50 km. The change of seismic velocities from anomalously low values at shallow depths to anomalously high values at greater depth may be the result of a downwelling or detachment of cold lithosphere and an upwelling of hotter upper mantle filling the space left by the downwelling lithosphere. Surface wave inversions often yield oscillatory solutions for the vertical distribution of shear velocity with length scales or amplitudes of the oscillations below the level of resolution, which might be a factor that could exaggerate the high velocity anomaly in the 130–170 km depth range, but we are confident that the reversal is real. First, the reversal is present in the phase velocities themselves; there is a switch from pronounced, low phase velocities in the 25–50 s range to locally high velocities at periods greater than 83 s. Second, this basic pattern of reversed anomalies has been

corroborated by previous body wave studies. Many investigators have reported low P and/or S wave velocities in the shallowmost mantle in this area [*Carder*, 1973; *Jones et al.*, 1994; *Savage et al.*, 1994; *Wernicke et al.*, 1996; *Jones and Phinney*, 1998; *Savage et al.*, 2003; *Boyd et al.*, 2004], although the geographic extent was not fully mapped due to limited station coverage. *Jones et al.* [1994] argued that there must be a paired, deeper, high velocity anomaly, because the traveltime anomalies from teleseismic events were small despite the low velocities in the shallow mantle. *Jones and Phinney* [1998] reported the hint of the top of such a body beginning at a depth of about 60 km from converted phases. *Biasi and Humphreys* [1992] found high P wave velocities at depths exceeding ~120 km in their tomographic image, but resolution was limited in this area due to poor station coverage. More recently, *Savage et al.* [2003] reported a large jump in P wave velocity at 75–100 km based on Pn waveforms, which would represent the bottom of the anomalously low-velocity zone and top of a high velocity anomaly, in agreement with the absence of the low-velocity anomaly at 90–110 km in our model. Finally, using an array of 24 broadband seismometers spanning the southern Sierra Nevada, *Boyd et al.* [2004] imaged a dipping high velocity anomaly at depths of 100 to 200 km underlying the shallow, low-velocity anomaly.

[31] In our images (Figure 10a), the high velocity anomaly beneath the eastern Sierra Nevada and Owens Valley may be connected to the high velocity anomaly beneath the southern Central Valley, in agreement with the conclusion of Boyd et al that the anomaly dips to the east. The existence and approximate lateral dimensions of the southern Central Valley anomaly, variously termed the Isabella anomaly or the Southern Great Valley anomaly, has long been known from P wave tomography [*Aki*, 1982; *Biasi and Humphreys*, 1992; *Benz and Zandt*, 1993; *Zandt and Carrigan*, 1993; *Jones et al.*, 1994; *Bijwaard et al.*, 1998]. All these studies as well as ours show that this high velocity anomaly within the low-velocity zone is not a slab-like body paralleling the Sierra Nevada, but is limited to a roughly circular area about 120 km in diameter. The depth extent was estimated to be on the order of 230 km in the body wave studies [*Biasi and Humphreys*, 1992; *Zandt and Carrigan*, 1993], but the depth is well constrained to be no greater than about 130 km (Figure 9g and 9h) by the reversal to anomalously slow phase velocities beginning at a period of about 83 s (Figure 6e). These slow phase velocities at long periods lead to anomalously low velocities beneath the southern Great Valley at depths exceeding 130 km, again corroborated by the detailed body wave tomography of *Boyd et al.* [2004]. The high velocity, southern Central Valley anomaly reaches a maximum amplitude of about 6% in the low-velocity zone at 90 to 110 km, essentially eliminating the contrast between lithosphere and asthenosphere at that point and thus compatible with a model of foundering or sinking of the lower lithosphere.

[32] The evidence for delamination of the lithosphere 4–8 Myr ago beneath the eastern Sierra Nevada is very strong. The absence of a crustal root, the low seismic velocities in the uppermost mantle, the change from crustal eclogitic xenoliths at depths to 65 km in the Miocene to peridotitic in the Quaternary defining an apparent adiabatic temperature gradient leading to temperatures as high as 1150°C near the base of the current crust [*Ducea and Saleeby*, 1996], the presence in peridotitic xenoliths of silicic melt inclusions that appear to be melted crust [*Ducea and Saleeby*, 1998], low electrical conductivities indicating the presence of melt [*Park*, 2004], the pulse of potassic volcanism about 3.5 Ma [*Manley et al.*, 2000], and depths of origin of Pliocene and Quaternary basaltic magmas ranging from about 40 to 120 km [*Feldstein and Lange*, 1999; *Wang et al.*, 2002; *Elkins-Tanton and Grove*, 2003] all indicate that the lower lithosphere, including the eclogitic root to the Sierra batholith, detached and sank, replaced by upwelling, asthenospheric mantle that underwent partial melting during its ascent. The Quaternary episode of basaltic volcanism beginning about 1.5 Ma is confined primarily to the eastern edge of the Sierra Nevada including Owens and Long Valley [*Manley et al.*, 2000] and coincides with the region of lowest velocities from 50 to 90 km (Figures 9d, 9e, and 11). This recent episode could represent upwelling in response to westernmost Basin and Range extension that extends to shallower depths here than elsewhere in the Basin and Range [*Wang et al.*, 2002] due to the prior removal of the lithosphere.

[33] One of the primary remaining questions is the fate of the delaminated lithosphere. A number of papers have focused on the high velocity Central Valley Anomaly as being the location of the downwelling track of the delaminated root [*Ruppert et al.*, 1998; *Saleeby et al.*, 2003; *Zandt*, 2003; *Zandt et al.*, 2004]. Noting the roughly cylindrical shape of this anomaly and its proximity to the circular shaped region of Pliocene mafic potassic volcanism (Figure 11), *Zandt* [2003] suggested that the lithosphere detached about 3.5 Ma and sank rapidly to the base of the asthenosphere, leaving a cold "tail" along its trail that is still downwelling. He noted that once a denser blob is detached, it should sink through a low-viscosity asthenosphere in less than 1 m.y., given viscosities of $10^{20}$ Pa s or less and reasonable estimates of the density contrast, so the original lower lithosphere has probably sunk out of range of the tomographic images. In this scenario, the tail has subsequently been displaced to the SSW from its origin beneath the area of potassic volcanism by the "mantle wind," part of the global asthenospheric counterflow directed to the SSW, rather than to the east as envisioned by those invoking flow driven by the subducted Farallon plate. *Zandt et al.* [2004] suggested that a locally thickened crust detected with receiver function techniques (also partially detected by *Fliedner and Ruppert* [1996]) represents lower crust viscously dragged downward by the dripping lithospheric mantle. *Saleeby et al.* [2003] presented a variant of this model in which the sinking lithospheric drip still contains the remnants of the original, convectively removed, subbatholith mantle lithosphere. Descent in their model presumably is slowed because the drip has never fully detached from the overlying lithosphere.

[34] We image with confidence only the southern part of the Pliocene field of potassic volcanism, but we show that lithospheric detachment was not limited to that area, continuing south as far as the latitude of the Central Valley Anomaly (Figures 9d and 9e). The burst of volcanism at ~3.5 Ma also was not confined just to the potassic area [*Manley et al.*, 2000]; it continued to the southern end of the detached area indicated by the low-velocity region we image at depths of 50 to 90 (Figure 11). The area of potassic

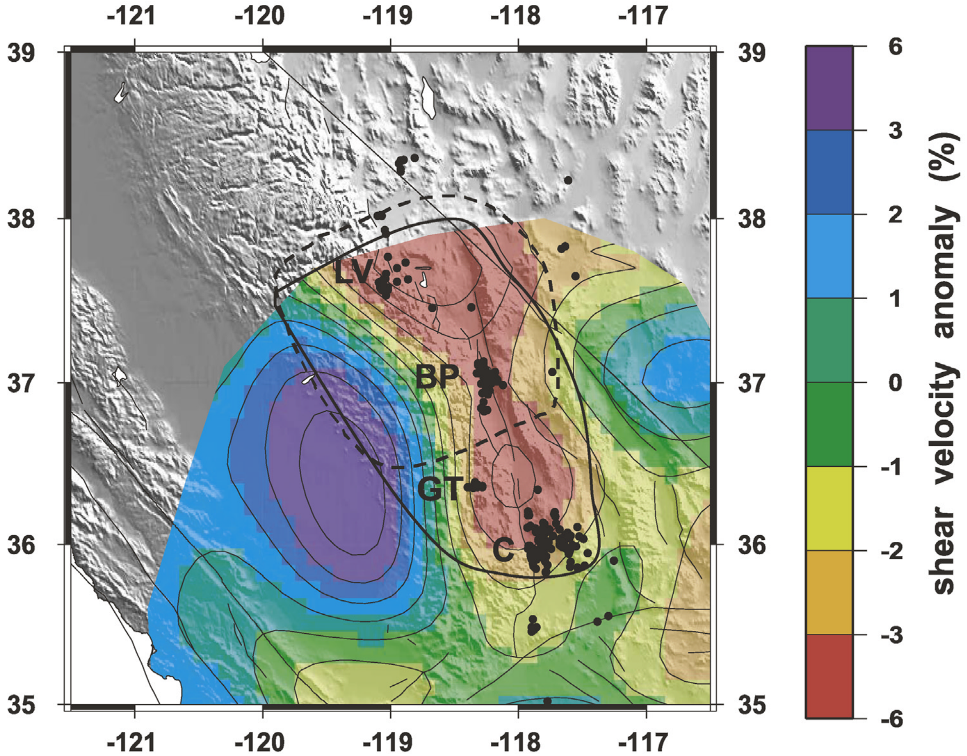

**Figure 11.** Distribution of volcanism (black dots) in southern Sierra Nevada during the Quaternary (1.5–0 Ma) period. Bold solid line outlines area with which Pliocene (chiefly 4–3 Ma) volcanism was prevalent; note that Quaternary volcanic fields (LV, Long Valley; BP, Big Pine; GT, Golden Trout; C, Coso) are all within area of Pliocene event. Dashed line outlines the area of Pliocene potassic volcanism 4–3 Ma [*Manley et al.*, 2000]. Colors show shear wave velocity anomalies at depths of 70–90 km as shown in Figure 9d. Note that the Quaternary volcanism coincides with the region of lowest velocities.

volcanism thus should not be taken as a unique indicator of where detachment took place. The potassic volcanism probably was triggered by detachment and consequent upwelling, but the potassic character was caused by an unusual composition of the upwelling mantle, which had apparently been previously metasomatized by a K-rich fluid [*van Kooten*, 1980; *Mukhopadhyay and Manton*, 1994; *Feldstein and Lange*, 1999; *Elkins-Tanton and Grove*, 2003]. The existence of high velocities directly beneath the delaminated region removes the motivation for identifying the Central Valley Anomaly as the destination of the delaminated lithosphere. The foundering lithosphere may sink vertically. Indeed, *Boyd et al.* [2004] identify regions of garnet pyroxenite extending deep into the mantle beneath the eastern Sierra Nevada on the basis of Vp/Vs ratios and attenuation, which they interpret as the delaminated, eclogitic, crustal root of the mountain range.

[35] In our image, it is not totally clear that the sinking beneath the eastern Sierra is physically connected to the foundering beneath the southern Central Valley. *Boyd et al.* [2004] show a continuous band of high P velocities dipping eastward from the Central Valley anomaly, but the S wave anomalies are not as uniform, with adjacent but perhaps distinct anomalies similar to the maxima beneath the Central Valley at 90 to 110 km and beneath the eastern Sierra at 130 to 170 km (Figures 9f, 9h, and 9i). The V-shaped cone of thickened crust observed beneath the Central Valley by *Zandt et al.* [2004] could either be caused by vertical sinking of the local lithosphere or by the viscous drag from an eastward plunging lithosphere. More coverage is needed to fully establish the shape beneath the region of Pliocene potassic volcanism to the NNE; coverage that should become available with the deployment of USArray.

### 7.2. Upwelling Beneath Salton Trough

[36] A moderately low-velocity anomaly is imaged beneath the Salton Trough at all depths down to 200 km. The recent surface wave tomographic study by *Tanimoto and Prindle Sheldrake* [2002] showed a similar low-velocity anomaly, but the limited period range prevented good depth resolution. This anomaly has also been imaged in previous P wave tomographic studies [*Raikes*, 1980; *Humphreys and Clayton*, 1990; *Biasi and Humphreys*, 1992; *Zhao et al.*, 1996]. Our observations of this low-velocity anomaly are similar to these studies in overall pattern. Our model has the largest velocity contrast from 70 to 110 km, with the center of the anomaly shifted to the west of the Salton Sea (Figures 9e and 9f). In the 90 to 130 km depth range, it is the slowest spot in southern California. At greater depths, the anomaly is elongated to the southeast and shifts to the southeast of the Salton Sea (Figures 9h and 9i).

[37] The extension of the Salton Trough anomaly into the low-velocity zone suggests that there may be a component of dynamic upwelling and melting associated with the extensional tectonics. Purely passive upwelling in response

to the extension and subsequent conductive cooling near the surface would not be expected to produce an anomaly in the asthenosphere, which should already follow an adiabatic gradient. The anomaly is more pronounced and distinct in our Rayleigh wave-derived S wave images than in most P wave tomographic studies [e.g., *Kohler et al.*, 2003], suggesting that melt probably plays an important role in creating it, because melt may more strongly affect S than P velocity.

### 7.3. Lithospheric Drips Beneath the Transverse Range

[38] The well-known upper mantle high-velocity anomaly beneath the Transverse Range [*Hadley and Kanamori*, 1977; *Raikes*, 1980; *Walck and Minster*, 1982; *Humphreys et al.*, 1984] is imaged from 50 to 150 km (Figure 10b). The high-velocity anomaly is most pronounced at the eastern and western ends of the Transverse Range. In the western end, the high velocity extends south to the offshore region. The scale of the high-velocity anomaly becomes smaller with increasing depth. Previous P wave tomographic studies [*Humphreys and Clayton*, 1990; *Zhao et al.*, 1996; *Kohler*, 1999; *Kohler et al.*, 2003] show that this feature is ~60 km thick and extends most deeply at the eastern end, in agreement with our observations, but the body wave studies indicate that the maximum depth is 200 to 250 km. Our images show that the high velocity only extends to about 150 km. One possible reason for this difference in the depth range between surface wave tomography and body wave tomography could be vertical smearing effects in the body wave tomography due to the nearly vertically incident angles of teleseismic body waves. Fundamental mode Rayleigh waves also lose resolving power at these depths, but we should be able to detect an anomaly extending from 150 to 250 km. Another possible difference in the depth range cited is simply interpretation of the images. *Kohler et al.* [2003] show that the high-velocity region broadens beneath 150 km, blending into an anomaly that covers much of southern California south of the Garlock fault. Therefore we conclude that the high-velocity anomalies extend only to about 150, or perhaps 170, km.

[39] The upper mantle high-velocity anomaly was interpreted by *Bird and Rosenstock* [1984] as a slab-like mantle convective downwelling induced by oblique convergent motion between Pacific plate and North American plate across the San Andreas fault, with the descending mantle decoupled from the crust. Subsequent authors [*Humphreys and Hager*, 1990; *Kohler*, 1999] argued that the entire subcrustal lithosphere on both sides of the convergent zone descends into the asthenosphere due to the gravity instability initiated by the convergence. In these simple models, the depth extent can be predicted kinematically by the integrated convergence since initiation of the bend in the San Andreas 5 to 10 m.y. ago. Our results suggest that instead of a simple, 2-D tabular form, the small scale convective instabilities take the form of localized drips that could draw in lower lithosphere from both along and across strike, breaking the direct kinematic predictability. At depths greater than 90 km, and perhaps even shallower, the Transverse Range anomaly breaks up into two roughly circular anomalies with a gap or near gap at about 118.5°W. The western anomaly, beginning under the Channel Islands, dips to the NNE, while the eastern anomaly is nearly vertical. *Humphreys and Clayton* [1990] and *Kohler et al.* [2003] show similar breaks in their P wave tomography images at the same longitude, although they do not find as strong a western anomaly, perhaps due to the scarcity of stations offshore. *Kohler and Davis* [1997] and *Kohler* [1999] report that there is a local zone of crustal thickening directly overlying the eastern drip, similar to that observed above the Central Valley anomaly, suggesting that crust and mantle are not completely decoupled. It is possible that other drips may have detached previously and sunk out of detection range.

### 7.4. Thin Crust and Cool Lithosphere Beneath the Borderlands

[40] Beneath the California Borderland, we observe high-velocity anomalies. From the Moho to 50 km, our model indicates high velocities south and east of Catalina and San Clemente islands. In this area, *Zhu and Kanamori* [2000] had no crustal control, because there are no stations where converted phases could be detected. Consequently, our interpolated crustal model has average crustal thicknesses of close to 30 km, but there is every reason to expect that the ~22 km thick crust adjacent to Catalina [*Nazareth and Clayton*, 2003] continues farther south along the coast, as the Catalina schist belt, representing middle crustal rocks uplifted and exposed during extension, continues at least as far as 31°S [*Bohannon and Geist*, 1998]. Thus the velocity anomalies in the uppermost mantle layer and lower crust simply indicate that model crust should be thinner in this area.

[41] From 50 to 70 km beneath the Borderlands, the shear velocity in the mantle is uniformly about 2.5% faster than in the reference model, or about 4.4 km/s (Figure 9d). This increase in velocity and the 3 to 4% increase in the northern Borderlands at depths greater than 70 km are compatible with the increase in lithospheric thickness inferred from SS waveforms and SS-S traveltimes assuming constant lid and low-velocity zone velocities [*Melbourne and Helmberger*, 2001]. Most of the extension in the Borderlands occurred in early to mid-Miocene, as the transfer to the Pacific plate occurred earlier here than farther inland [*Bohannon and Geist*, 1998], giving more time for the lithosphere to cool. There may also be fragments of oceanic lithosphere captured in the Borderlands, which, together with the expected lower temperatures, could account for the higher velocities in the lithosphere. At the northern end of the Borderlands, in the vicinity of the Channel Islands, the lithospheric anomaly merges with the deeper (>90 km) anomaly described above that we associate with a mantle drip beneath the western end of the Transverse Ranges.

### 7.5. Peninsular Range Drip and Mojave Anomaly

[42] All of the features described above in the Sierra Nevada, Central Valley, Transverse Ranges, Salton Trough and Borderlands regions have been detected and characterized in previous seismological investigations using other techniques. One advantage of Rayleigh wave tomography is that it provides more uniform resolution that is somewhat less dependent on the local density of seismic stations than body wave tomography. Having established the credibility of the Rayleigh wave tomography by comparison with known features, we focus here on two deep anomalies in

regions of relatively sparse station coverage that have previously escaped detection: a high-velocity anomaly beneath the Peninsular Range and a low-velocity anomaly beneath the Mojave desert.

[43] Beneath the northern Peninsular Range, there is a high-velocity anomaly at depths greater than about 130 km (Figures 9h, 9i, and 10c). In our phase velocity maps, this is the strongest anomaly at the longest periods (Figure 6g), exceeding 3%, so we are probably just detecting the top of the body and cannot establish its vertical extent. Our modeling may also underestimate the depth to the top; because we restrict lateral velocity variations to the upper 200 km, a deeper anomaly that is still within the range of detection will be forced to shallower levels.

[44] The Peninsular Range anomaly may represent a sinking drip or blob that has completely detached from the overlying lithosphere in a process that may be very similar to the delamination of the eastern root of the Sierra Nevada. The Peninsular Ranges Batholith along with the Sierra Nevada batholith formed the continuous, Mesozoic California Batholith that has subsequently been disrupted by strike-slip faulting and extension in southern California [e.g., *Silver and Chappell*, 1988]. Like the Sierra Nevada batholith, the eastern Peninsular Ranges Batholith probably was underlain by an eclogitic residual root [*Gromet and Silver*, 1987]. An eclogitic root forms a gravitationally metastable layer within the lithosphere that, in the Sierra Nevada, delaminated only after extension began in the adjacent Basin and Range province. Adjacent extension could also be the trigger for delamination of the lithosphere beneath the Peninsular Range, but extension began earlier at 15–20 Ma in the Borderlands region [*Luyendyk*, 1991; *Bohannon and Geist*, 1998] before switching eastward to the Gulf of California, so delamination may have begun sooner and progressed further. Perhaps upwelling of the asthenosphere replacing the delaminated lithosphere has ceased at shallow levels, or never reached as shallow as the Sierra Nevada detachment, because we do not see the pronounced low-velocity anomalies that are present beneath the eastern edge of the Sierra Nevada at 50 to 70 km. However, perhaps the low-velocity region 70 to 110 km deep west of the Salton Sea and near the San Jacinto fault represents such an upwelling zone that enhances the upwelling associated with extension in the Salton Trough area, displacing it westward. Models show that lithospheric delamination does not necessarily produce melting. The occurrence of melting is dependent on the viscosity structure of the lithosphere and the release of volatiles from the descending drip (L. T. Elkins-Tanton, Continental magmatism, volatile recycling, and a heterogeneous mantle caused by lithospheric Rayleigh-Taylor instabilities, submitted to *Journal of Geophysical Research*, 2005).

[45] The second new feature is a low-velocity anomaly centered at about 35.5°N, 117°W in the northern Mojave desert. Like the anomaly beneath the Peninsular Range, we see it clearly in the longest-period phase velocities (Figures 6f and 9g) and thus can only resolve the top of the anomalous body (Figures 9h and 9i). It is not clear what tectonic processes created this anomaly, but it may represent convective upwelling that is required to balance downwelling elsewhere in the system. However, adiabatic upwelling of peridotite should not produce low velocities and melting at this depth. It is possible that it is a sliver of delaminated eclogitic crust trapped beneath the asthenosphere; eclogite at this depth would be expected to have lower shear velocity and lower melting temperature than the surrounding periodite [*Anderson*, 2005].

## 8. Azimuthal Anisotropy

[46] Shear wave splitting measurements at many stations in southern California [*Savage and Silver*, 1993; *Özalaybey and Savage*, 1995; *Liu et al.*, 1995; *Polet and Kanamori*, 2002] show a nearly consistent fast direction close to E-W with splitting time ranging from 0.75 to 1.5 s. However, because the ray paths of SKS phases used in the analysis are nearly vertical, the depth distribution of anisotropy cannot be inferred from the shear wave splitting data alone. Taking advantage of the sensitivity of Rayleigh waves of different periods to structure at different depths and the fact that the fast direction for Rayleigh wave propagation should be the same as the fast direction for shear wave splitting if the anisotropic structure has a horizontal symmetry axis with orthorhombic (or higher order) symmetry, we can solve for the vertical distribution of anisotropy.

[47] In the inversion for phase velocities, we simultaneously solve for isotropic term $A_0$ and azimuthal term $A_1$ and $A_2$ (equation (1)). The peak-to-peak anisotropy is $2(A_1(\omega)^2 + A_2(\omega)^2)^{1/2}/A_0(\omega)$ and the fast direction is $\frac{1}{2}\tan^{-1}(A_2(\omega)/A_1(\omega)$. Standard errors for the strength and fast direction can be calculated from the variation of $A_1$ and $A_2$ using an error propagation technique [*Clifford*, 1975]. Mathematically, we can solve for the 2-D variation of anisotropy on the scale of a grid cell. However, when we introduce 2-D anisotropy terms $A_1$ and $A_2$, there are three times as many parameters as there are for isotropic phase velocity $A_0$ alone, and they are not resolved very well. Because the shear wave splitting directions are nearly constant, it is reasonable as a first approximation to assume that anisotropy is uniform in the entire southern California region while isotropic phase velocities are allowed to vary laterally. Later we consider variations based on prescribed geographic regions to test specific hypotheses.

[48] The average azimuthal anisotropy at various periods in southern California is shown in Figure 12. Because we assume homogeneity, the sensitivity kernel is simply proportional to path length within the study area. The standard deviations of amplitude have been plotted as error bars, which are ~0.15% at periods less than 67s and increase with period to 0.7% at 143 s. The standard derivations of the fast directions are ~3° at periods less than 67s and reach a maximum of greater than 10° at the longest periods. At periods from 25 to 100 s, the strength is nearly uniform and averages about 1.7% peak-to-peak amplitude, about half the amplitude of the azimuthal anisotropy in young seafloor in the Pacific found within local arrays [*Forsyth et al.*, 1998; D. S. Weeraratne et al., Rayleigh wave tomography of the oceanic mantle beneath intraplate seamount chains in the South Pacific, submitted to *Journal of Geophysical Research*, 2006]. At longer periods, the strength decreases to below 1%. The variation of fast direction with period is small. At periods less than 60 s, the average direction is about N82°W, rotating to slightly south of east at longer periods, but with larger uncertainty. The change in anisot-

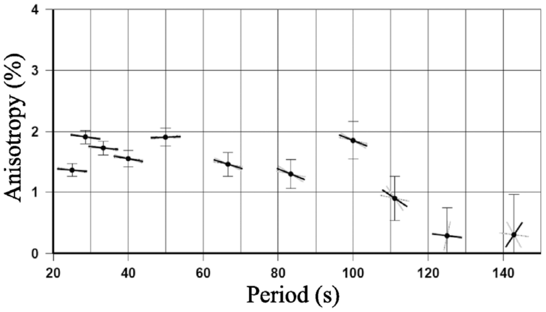

**Figure 12.** Variations of average azimuthal anisotropy with period in southern California. The vertical solid bars with caps represent plus or minus one standard deviation of amplitude. Fast directions of azimuthal anisotropy are indicated by the orientations of black bars as if in a map view with north up on the diagram; plus and minus one standard deviation in direction are shown as two gray bars at each period. Note that standard deviations for the fast directions are very small at short periods. Amplitudes represent contrast between fast and slow direction as percentage of average phase velocity.

ropy with period suggests that there may be a somewhat different and weaker orientation in the asthenosphere than the lithosphere, but the change in direction is small enough that it would be difficult to detect with azimuthal variations in shear wave splitting, consistent with the single-layer anisotropy models proposed for southern California [*Liu et al.*, 1995; *Polet and Kanamori*, 2002; *Davis*, 2003].

[49] There is a potential trade-off between anisotropy terms $A_1$ and $A_2$ and lateral variations in the azimuthally averaged velocity term $A_0$ when they are jointly inverted. In principle, in ray theory the anisotropic effects on traveltime can be perfectly modeled by allowing strong lateral variations in isotropic velocities on a distance scale significantly smaller than the separation between stations. In this study, the lateral variations of phase velocities are limited by smoothing with a 65-km characteristic length, which, combined with the averaging inherent in the Fresnel zones of the response kernels and the relatively high density of stations, prevents short-wavelength velocity variations from mimicking the effects of azimuthal anisotropy. With our excellent azimuthal distribution of sources, we find no significant difference between the lateral variations in $A_0$ inverted without azimuthal terms, shown in Figure 6, and $A_0$ in models that include the azimuthal terms. Thus there is no indication that neglect of anisotropy introduces artifacts into our phase velocity maps.

[50] At long periods, however, it is possible that lateral variations in structure influence the apparent anisotropy. For example, at 100 s the wavelength is about 400 km, which is significantly larger than the scale of velocity variations we find and greater than the width of features like the Sierra Nevada, Peninsular Range, and Great Valley. The variation of phase velocities at long periods could behave somewhat more like a laterally uniform region with shape-preferred anisotropy than a laterally heterogeneous region, just like layered sediments produce effective transverse anisotropy when the layering is on a scale of less than one wavelength. If that were the case, we would underestimate the lateral heterogeneity and overestimate the azimuthal anisotropy due to truly small-scale structure such as lattice-preferred orientation of crystals or alignment of cracks. The change of fast directions at the longest periods to being more parallel to the plate boundary and the dominant tectonic trends could possibly be due to this layering effect on anisotropy instead of intrinsic anisotropy, although the fact that the planform of the anomalies we do resolve tends to be irregular or circular in shape rather than linear suggests that it may not be an important effect. In order to quantitatively evaluate the tradeoff, we need to investigate the effects of lateral heterogeneities on apparent anisotropy of long-period Rayleigh waves by modeling Rayleigh wave propagation through laterally heterogeneous media with the full elastic wave equations in models that simulate potential structures in southern California, which is beyond the scope of this current study.

[51] The Rayleigh wave azimuthal anisotropy and the shear wave splitting delay times between 0.75 and 1.5 s require that anisotropy extend through both lithosphere and asthenosphere. Assuming 4% anisotropy for upper mantle materials, *Polet and Kanamori* [2002] estimated an anisotropic layer about 100–200 km thick, according to the range of delay times. Combining information from P wave polarization [*Schulte-Pelkum et al.*, 2001], Pn times [*Hearn*, 1996], Rayleigh and Love velocities, and SKKS and SKS splitting, *Davis* [2003] concluded that anisotropy is distributed throughout the upper 200 km of the mantle up to the base of the crust. In our study, the strength of azimuthal anisotropy is ~1.7% at periods shorter than 100 s and less than 1% at longer periods. Rayleigh waves at periods shorter than 50 s are primarily sensitive to the lithosphere, including the crust. The upper crust is anisotropic, probably due to the orientation of cracks, but the maximum splitting times in the upper crust in the Los Angeles basin area are only about 0.12 s and the fast direction is approximately N-S [*Li et al.*, 1994], orthogonal to the fast direction observed for teleseismic wave splitting and azimuthal anisotropy. The lower crust is likely to be more isotropic. To yield 1.7% anisotropy of the short-period Rayleigh waves requires 2–3% shear wave anisotropy in the mantle part of the lithosphere. The contribution to shear wave splitting from the lithosphere from 30 to 90 km is thus approximately 0.25 to 0.4 s. The degree of anisotropy in the asthenosphere should be significantly smaller and decrease with increasing depth since Rayleigh waves at periods longer than 100 s are primarily sensitive to the asthenosphere. Taking an average value of ~1% requires that the nonlithospheric contribution to splitting extend over a depth range on the order of 300 km to produce a total average splitting of about 1.1 s.

[52] *Liu et al.* [1995] first argued that the cause of the E-W fast orientation might be related to late Cenozoic N-S contraction in southern California as manifested in the creation of the Transverse Ranges and contraction in the Mojave block [*Bartley et al.*, 1990]. In order to more quantitatively evaluate the relationship between the fast directions with the direction of compressional stresses, *Polet and Kanamori* [2002] plotted the fast directions of anisotropy and the maximum compressive stress directions from the world Stress Map together. They found that the fast direction is nearly orthogonal to the maximum compressive stress in southern California and argued that this perpen-

dicularity is consistent with the alignment of the *a* axis of olivine perpendicular to the direction of lithospheric shortening. This mechanism, however, does not explain the larger contribution to splitting from the asthenosphere, which is unlikely to be directly coupled to any lithospheric shortening. Indeed, in central California in the vicinity of the major strike-slip faults of the Bay area, two layers of anisotropy are required to explain the splitting [*Savage and Silver*, 1993; *Özalaybey and Savage*, 1995; *Liu et al.*, 1995]; although it is difficult to uniquely resolve the directions [*Hartog and Schwartz*, 2001], the fast direction in the upper layer may be aligned parallel to the San Andreas fault and the lower, sublithospheric layer E-W. In southern California, two directions are not resolved, even close to the San Andreas [*Polet and Kanamori*, 2002; *Davis*, 2003].

[53] One of most likely causes of anisotropy in the asthenosphere is the flow-induced, lattice-preferred orientation of olivine. *Özalaybey and Savage* [1995] argued that asthenospheric flow in the slabless window left behind the Farallon plate could create the E-W fast direction. *Silver and Holt* [2002], noting the small change in orientation of SKS fast directions from slightly clockwise of E-W near the coast to ENE in the western Basin and Range including Walker Lane [*Polet and Kanamori*, 2002], attributed the change in direction to the different motions of the Pacific and North American plates relative to flow in the underlying mantle. They predicted an eastward mantle flow with velocity 5.5 ± 1.5 centimeters per year; flow which could be produced by the sinking Farallon slab. We are not convinced that the change in orientation occurs at the plate boundary. It seems more to be a change associated with extension in the Basin and Range province. Following the model of Silver and Holt, we performed an experiment in which we subdivided the region into two areas divided by the San Andreas fault in which the azimuthal anisotropy of Rayleigh waves is allowed to be different. We found no significant difference in anisotropy in the two regions.

[54] It is perhaps surprising that the shear wave splitting orientation is so uniform if there are convective upwellings and downwellings in the asthenosphere, as indicated by our surface wave tomography and previous body wave studies, that should alter the local flow directions. Perhaps the uniformity in direction is caused by a relatively uniform lithospheric fabric and the decrease in amplitude of the average azimuthal anisotropy at longer periods is associated with a more chaotic pattern in the asthenosphere. The variations in amplitude of splitting and the smaller variations in direction could be caused by local variations in the relative contributions of asthenosphere and lithosphere. *Polet and Kanamori* [2002] noted that they could not find any high-quality, split SKS phases at stations ISA and MLAC above the Isabella or Central Valley anomaly and the Mammoth Lakes/Long Valley anomalies, respectively. Thus there may be local disruptions of the overall shearing flow between the lithosphere and deeper mantle due to small scale convection, but if the anisotropic layer extends to depths as great as 400 km and these convective features are primarily drips or local upwellings, then they may occupy a small fraction of the total volume of the anisotropic layer and cause only relatively minor perturbations in the overall pattern of flow associated with plate motion.

## 9. Conclusions

[55] Using Rayleigh wave phase and amplitude data, we have solved for azimuthal anisotropy and lateral variations in phase velocity in southern California. The use of finite frequency response kernels and an approximate representation of the incoming wavefields, coupled with a high density of broadband stations and excellent azimuthal distribution of sources allows unprecedented resolution to periods as long as 140 s. A one-dimensional shear wave velocity profile based on the average phase velocities shows a low-velocity zone in the upper mantle underlying a high-velocity lithospheric lid. The velocity contrast between them is about 7%. The thickness of lithosphere is ~90 km, but the average shear velocity in the lid of 4.35 km/s is significantly less than in other regions with comparable thickness, indicating average temperatures in the lid are probably several hundred degrees hotter and that there is likely to be melt present in the asthenosphere.

[56] In the uppermost mantle, there is a low-velocity anomaly beneath the eastern edge of the southern Sierra Nevada and the adjoining Walker Lane region that is directly underlain by a high-velocity anomaly. This velocity pattern supports the argument that the lithosphere detached from the crust and sank into the surrounding mantle and the lower, hotter asthenosphere upwelled and filled the space left by the sinking lithosphere, undergoing partial melting as it rose. The high-velocity anomaly at depth may be connected to a shallower high-velocity anomaly beneath the southern Central Valley forming an eastward dipping structure. The well-known, high-velocity anomaly associated with downwelling lithosphere beneath the Transverse Range is imaged extending down to ~150 km, rather than the 200 to 250 km suggested in previous studies. We also image the top of a high-velocity anomaly beneath the northern Peninsular Range that may be a lithospheric drip that has fully detached from the overlying plate. A moderate low-velocity anomaly is observed beneath the Salton Trough region associated with the extensional tectonics, but at shallow levels it may also represent upwelling replacing the delaminated lithosphere beneath the Peninsular Range. Another deep anomaly, a north-south trending, low-velocity body, is found beneath the northeastern Mojave Desert. The shape of these anomalies and their association with tectonic and volcanic features on the surface strongly support the existence of small-scale convection beneath southern California and suggest that the dominant form of convection is in the form of 3-D lithospheric drips and asthenospheric upwellings rather than 2-D, slab-like sheets.

[57] Azimuthal anisotropy is found in a joint inversion including lateral variations of phase velocities. The strength of anisotropy is ~1.7% at periods shorter than 100 s and decreases to below 1% at longer periods. This strength combined with the measurements of shear wave splitting time from other studies constrain the thickness of the anisotropic layer to be more than 300 km. The average fast direction is nearly E-W, which is consistent with shear wave splitting measurements. The E-W fast direction is attributed partially to the N-S compressive stress in the lithosphere

and partially to asthenospheric flow at depth, which may be locally disrupted by convective features.

## Appendix A: Corrections for Station Instrumental Responses and Local Site Responses

[58] A key element in our study is the correction for instrument responses. The 40 broadband stations consist of several different types of seismometers. It often may not be properly appreciated, but just as stations frequently have misoriented horizontal components [*Schulte-Pelkum et al.*, 2001], they also commonly have misreported or miscalibrated response functions. In every study we have performed to date that has involved multiple instrument types (MELT Experiment, northeastern United States/MOMA, Colorado/Rocky Mountain Front, Tanzania), we have found that the instrument response parameters reported for at least one of the instrument types has been incorrect. We first use the published responses to correct all seismograms to the response of a common instrument type. Incorrect amplitudes and phases responses are then detectable through amplitude mismatches or careful comparison of waveforms at adjacent stations. Then, as part of our tomographic inversion for phase velocities and wavefield parameters, we group stations with same instrumental responses together and solve for an amplitude correction and phase correction for that group of seismometers as a function of frequency (keeping one type fixed as the standard). We then correct all the seismograms to the standard response and repeat the inversion, this time allowing a separate amplitude response for every station, because individual stations sometimes do not function in the same way as others of the same type. In principle, if there were no other factors affecting amplitude, one could solve for corrections to one station of a pair of stations using just two earthquake sources producing waves traveling in opposite directions along a great circle path between the two stations. In practice, using many sources from a wide range of azimuths, we find amplitude corrections resolved with standard deviations of just a few percent, including tradeoffs with focusing, wavefield parameters and attenuation.

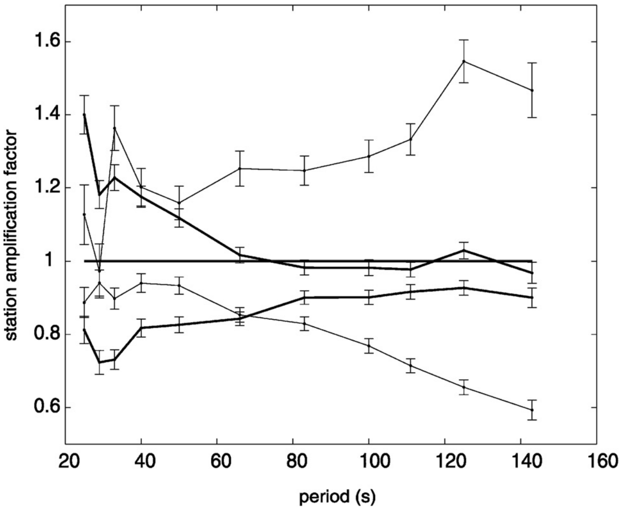

**Figure A1.** Variation of station/site responses with period for four stations. Each line represents one station. Error bars indicate plus or minus one standard deviation. The nominal instrumental response has been removed before the inversion. Two examples of the typical pattern of station/site responses are shown as bold lines, with relatively large deviations at short periods gradually approaching 1.0 at long periods. The responses for two anomalous stations are shown as thin lines. These anomalous patterns are probably caused by incorrect instrumental response corrections.

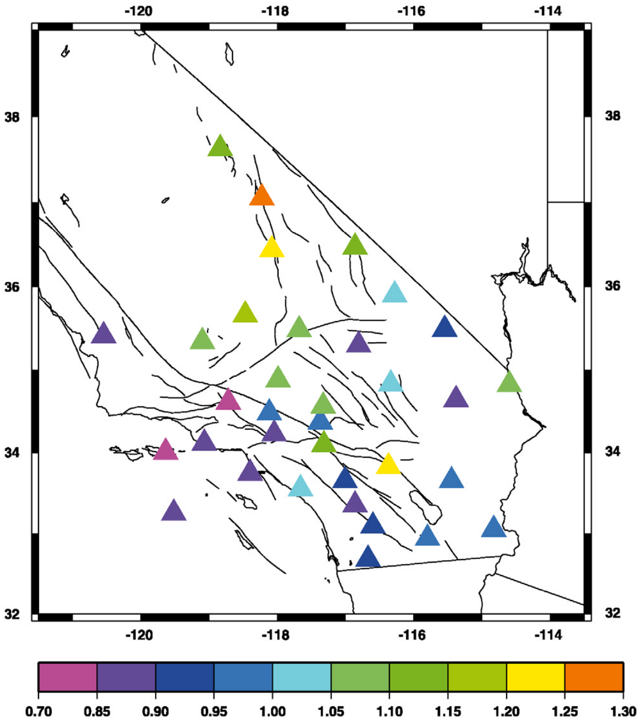

**Figure A2.** Map view of station/site amplitude responses for Rayleigh waves at a period of 25 s. The variation in amplitude is up to a factor of 2, with the lowest amplitudes near the coast and in southernmost California and the highest amplitudes in the Owens Valley/Long Valley region. Stations with anomalous amplitude patterns as a function of period (Figure A1) have been eliminated from this map.

[59] Typically, the second stage solutions for individual station responses will deviate from the average, standard response by up to about 20% at short periods (∼25 s) and then gradually approach a ratio of ∼1.0 at long periods (>∼100 s) (Figure A1). We attribute this pattern to local site responses rather than instrument problems. At longer wavelengths, the wave averages over a broader area and greater depth range and the site responses are expected to become more uniform. Amplification of surface waves at very short periods (<10 s), of course, is a very well known and important factor in earthquake hazards [e.g., *Shapiro et al.*, 1997] but has largely been ignored at longer periods. Occasionally, we find a station where the response does not approach 1.0 at long periods, which we interpret as an incorrect response function. We then isolate this station from others of its group and recalculate the responses for each instrument type, with a separate response for that particular instrument. (In addition to solving for amplitude correction factors, if there is any indication of incorrect response, we also solve for phase correction factors.) This procedure loses any information about site response for that

problem station, but it does preserve the correction needed for reliable determination of variations in amplitude for a wave propagating across the array. If there is any indication that the response of a particular station is not uniform with time, we drop that station from our analysis entirely. After identifying problematic stations, there is a clear geographic pattern to the apparent site responses at short periods (Figure A2) that correlates with tectonic province and with the pattern of phase velocities. These site responses carry information about local structure that we will explore in a future study. Numerical experiments on the propagation of Rayleigh waves through synthetic, heterogeneous media demonstrate that the single scattering approximations that we use in assessing the amplitude effects of focusing within the array do not take into account the local site response within the anomaly itself, although the apparent response may also be affected by inadequate representation of back-scattering [*Yang and Forsyth*, 2006]. The important point for this study is that the station correction terms account for instrument and site effects not incorporated in other parameters of the model.

[60] **Acknowledgments.** The seismic data used in this study were obtained from the Southern California Earthquake Data Center (SCEDC). We would like to thank Frederik J. Simons and two anonymous reviewers for providing critical and constructive comments. This research was supported by National Science Foundation grants OCE-9911729 and EAR-0510621.

## References

Aki, K. (1982), Three-dimensional seismic inhomogeneities in the lithosphere and asthenosphere: Evidence for decoupling in the lithosphere and flow in the asthenosphere, *Rev. Geophys.*, *20*, 161–170.

Anderson, D. L. (2005), The plate and plume paradigms, *Geol. Soc. Am. Abstr. Programs*, *37*(7), 312.

Atwater, T. (1998), Plate tectonic history of southern California with emphasis on the western Transverse Ranges and Santa Rosa Island, in *Contributions to the Geology of the Northern Channel Islands, Southern California*, edited by P. W. Weigang, pp.1–8, Am. Assoc. of Pet. Geol., Pac. Sect., Bakersfield, Calif.

Bartley, J. M., A. F. Glazner, and E. R. Schermer (1990), North-south contraction of the Mojave block and strike-slip tectonics in southern California, *Science*, *248*, 1398–1401.

Benz, H. M., and G. Zandt (1993), Teleseismic tomography: Lithospheric structure of the San Andreas fault system in northern and central California, in *Seismic Tomography: Theory and Practice*, edited by H. M. Iyer and K. Hirahara, pp. 440–465, CRC Press, Boca Raton, Fla.

Biasi, G. P., and E. D. Humphreys (1992), P-wave image of the upper mantle structure of central California and southern Nevada, *Geophys. Res. Lett.*, *19*, 1161–1164.

Bijwaard, H., W. Spakman, and E. R. Engdahl (1998), Closing the gap between regional and global travel time tomography, *J. Geophys. Res.*, *103*, 30,055–30,078.

Bird, P., and R. W. Rosenstock (1984), Kinematics of present crust and mantle flow in southern California, *Geol. Soc. Am. Bull.*, *95*, 946–957.

Bohannon, R. G., and E. Geist (1998), Upper crustal structure and Neogene tectonic development of the California continental borderland, *Geol. Soc. Am. Bull.*, *110*, 779–800.

Boyd, O. S., C. H. Jones, and A. F. Sheehan (2004), Foundering lithosphere imaged beneath the southern Sierra Nevada, California, USA, *Science*, *305*, 660–662.

Carder, D. S. (1973), Trans-California seismic profile, Death Valley to Monterrey Bay, *Bull. Seismol. Soc. Am.*, *63*, 571–586.

Clifford, A. A. (1975), *Multivariate Error Analysis*, John Wiley, Hoboken, N. J.

Crough, S. T., and G. A. Thompson (1977), Upper mantle origin of Sierra Nevada uplift, *Geology*, *5*, 396–399.

Davis, P. M. (2003), Azimuthal variation in seismic anisotropy of the southern California uppermost mantle, *J. Geophys. Res.*, *108*(B1), 2052, doi:10.1029/2001JB000637.

Debayle, E., and M. Sambridge (2004), Inversion of massive surface wave data sets: Model construction and resolution assessment, *J. Geophys. Res.*, *109*, B02316, doi:10.1029/2003JB002652.

Ducea, M. N., and J. B. Saleeby (1996), Buoyancy sources for a large, unrooted mountain range, the Sierra Nevada, California: Evidence from xenolith thermobarometry, *J. Geophys. Res.*, *101*, 8229–8244.

Ducea, M. N., and J. B. Saleeby (1998), Crustal recycling beneath continental arcs: Silica-rich glass inclusions in ultramafic xenoliths from the Sierra Nevada, California, *Earth Planet. Sci. Lett.*, *156*, 101–116.

Elkins-Tanton, L. T., and T. L. Grove (2003), Evidence for deep melting of hydrous, metasomatized mantle: Pliocene high potassium magmas from the Sierra Nevadas, *J. Geophys. Res.*, *108*(B7), 2350, doi:10.1029/2002JB002168.

Faul, U. H., and I. Jackson (2005), The seismological signature of temperature and grain size variations in the upper mantle, *Earth Planet. Sci. Lett.*, *234*, 119–234.

Feldstein, S. N., and R. A. Lange (1999), Pliocene potassic magmas from the Kings River region, Sierra Nevada, California: Evidence for melting of a subduction-modified mantle, *J. Petrol.*, *40*, 1301–1320.

Fliedner, M. M., and S. Ruppert (1996), Three-dimensional crustal structure of the southern Sierra Nevada from seismic fan profiles and gravity modeling, *Geology*, *24*, 367–370.

Forsyth, D. W., and A. Li (2005), Array-analysis of two-dimensional variations in surface wave phase velocity and azimuthal anisotropy in the presence of multi-pathing interference, in *SeismicEarth: Array Analysis of Broadband Seismograms*, *Geophys. Monogr. Ser.*, vol. 157, edited by A. Levander and G. Nolet, pp. 81–97, AGU, Washington, D. C.

Forsyth, D. W., S. Webb, L. Dorman, and Y. Shen (1998), Phase velocities of Rayleigh waves in the MELT experiment on the East Pacfic Rise, *Science*, *280*, 1235–1238.

Friederich, W. (1998), Wave-theoretical inversion of teleseismic surface waves in a regional network: Phase velocity maps and a three-dimensional upper-mantle shear-wave velocity model for southern Germany, *Geophys. J. Int.*, *132*, 203–225.

Friederich, W., and E. Wielandt (1995), Intepretation of seismic surface waves in regional networks: Joint estimation of wavefield geometry and local phase velocity: Method and tests, *Geophys. J. Int.*, *120*, 731–744.

Friederich, W., E. Wielandt, and S. Stange (1994), Non-plane geometries of seismic surface wavefields and their implications for regional-scale surface wave tomography, *Geophys. J. Int.*, *119*, 931–948.

Grand, S. P., and D. V. Helmberger (1984), Upper mantle shear structure of North America, *Geophys. J. R. Soc. London*, *76*, 399–438.

Gromet, L. P., and L. T. Silver (1987), REE variations across the Peninsular Ranges batholith: Implications for batholithic petrogenesis and crustal growth in magmatic arcs, *J. Petrol.*, *28*, 75–125.

Hadley, D. M., and H. Kanamori (1977), Seismic structure of the Transverse Ranges, California, *Geol. Soc. Am. Bull.*, *88*, 1461–1478.

Hartog, R., and S. Y. Schwartz (2001), Depth-dependent mantle anisotropy below the San Andreas fault system: Apparent splitting parameters and waveforms, *J. Geophys. Res.*, *106*, 4155–4167.

Hearn, T. M. (1996), Anisotropic *Pn* tomography in the western United States, *J. Geophys. Res.*, *101*, 8403–8414.

Humphreys, E. D., and R. W. Clayton (1990), Tomographic image of the southern California mantle, *J. Geophys. Res.*, *95*, 19,725–19,746.

Humphreys, E. D., and B. H. Hager (1990), A kinematic model for the late Cenozoic development of southern California crust and upper mantle, *J. Geophys. Res.*, *95*, 19,747–19,762.

Humphreys, E. D., R. W. Clayton, and B. H. Hager (1984), A tomographic image of mantle structure beneath southern California, *Geophys. Res. Lett.*, *11*, 625–627.

Jackson, I., J. D. Fitz Gerald, U. H. Faul, and B. H. Tan (2002), Grain-size-sensitive seismic wave attenuation in polycrystalline olivine, *J. Geophys. Res.*, *107*(B12), 2360, doi:10.1029/2001JB001225.

Jones, C. H., and R. A. Phinney (1998), Seismic structure of the lithosphere from teleseismic converted arrivals observed at small arrays in the southern Sierra Nevada and vicinity, California, *J. Geophys. Res.*, *103*, 10,065–10,090.

Jones, C. H., H. Kanamori, and S. W. Roecker (1994), Missing roots and mantle "drips": Regional *Pn* and teleseismic arrival times in the southern Sierra Nevada and vicinity, California, *J. Geophys. Res.*, *99*, 4567–4601.

Kohler, M. D. (1999), Lithospheric deformation beneath the San Gabriel Mountains in the southern California Transverse Range, *J. Geophys. Res.*, *104*, 15,025–15,041.

Kohler, M. D., and P. M. Davis (1997), Crustal thickness variations in southern California from Los Angeles Region Seismic Experiment passive phase teleseismic travel times, *Bull. Seismol. Soc. Am.*, *87*, 1330–1344.

Kohler, M. D., H. Magistrale, and R. W. Clayton (2003), Mantle heterogeneities and the SCEC reference three-dimensional seismic velocity model version 3, *Bull. Seismol. Soc. Am.*, *93*, 757–774.

Li, A., D. W. Forsyth, and K. M. Fischer (2003), Shear velocity structure and azimuthal anisotropy beneath eastern North American from Rayleigh wave inversion, *J. Geophys. Res.*, *108*(B8), 2362, doi:10.1029/2002JB002259.

Li, Y.-G., T.-L. Teng, and T. L. Henyey (1994), Shear wave splitting observations in the northern Los Angeles basin, southern California, *Bull. Seismol. Soc. Am.*, *84*, 307–323.

Liu, H., P. M. Davis, and S. Gao (1995), SKS splitting beneath southern California, *Geophys. Res. Lett.*, *22*, 767–770.

Luyendyk, B. P. (1991), A model for Neogene crustal rotations, transtension, and transpression in southern California, *Geol. Soc. Am. Bull.*, *103*, 1528–1536.

Magistrale, H., S. Day, R. W. Clayton, and R. Graves (2000), The SCEC southern California reference three-dimensional seismic velocity model version 2, *Bull. Seismol. Soc. Am.*, *90*, S65–S76.

Manley, C. R., A. F. Glazner, and G. L. Farmer (2000), Timing of volcanism in the Sierra Nevada of California: Evidence for Pliocene delamination of the batholithic root?, *Geology*, *28*, 811–814.

Melbourne, T., and D. Helmberger (2001), Mantle control of plate boundary deformation, *Geophys. Res. Lett.*, *28*, 4003–4006.

Mukhopadhyay, B., and W. I. Manton (1994), Upper-mantle fragments from beneath the Sierra Nevada batholith: Partial fusion, fractional crystallization, and metasomatism in a subduction-related ancient lithosphere, *J. Petrol.*, *35*, 1417–1450.

Nazareth, J. J., and R. W. Clayton (2003), Crustal structure of the Borderland-continent transition zone of southern California adjacent to Los Angeles, *J. Geophys. Res.*, *108*(B8), 2404, doi:10.1029/2001JB000223.

Nishimura, C. E., and D. W. Forsyth (1989), The anisotropic structure of the upper mantle in the Pacific, *Geophys. J.*, *96*, 203–229.

Özalaybey, S., and M. K. Savage (1995), Shear wave splitting beneath western United States in relation to plate tectonics, *J. Geophys. Res.*, *100*, 18,135–18,149.

Park, S. K. (2004), Mantle heterogeneity beneath eastern California from magnetotelluric measurements, *J. Geophys. Res.*, *109*, B09406, doi:10.1029/2003JB002948.

Polet, J., and H. Kanamori (1997), Upper-mantle shear velocities beneath southern California determined from long-period surface waves, *Bull. Seismol. Soc. Am.*, *87*, 200–209.

Polet, J., and H. Kanamori (2002), Anisotropy beneath California: Shear wave splitting measurements using a dense broadband array, *Geophys. J. Int.*, *149*, 313–327.

Pollitz, F. F. (1999), Regional velocity structure in northern California from inversion of scattered seismic surface waves, *J. Geophys. Res.*, *104*, 15,043–15,072.

Press, F. (1956), Determination of crustal structure from phase velocity of Rayleigh waves, I, Southern California, *Geol. Soc. Am.*, *67*, 1647–1658.

Raikes, S. A. (1980), Regional variations in upper mantle structure beneath southern California, *Geophys. J. R. Astron. Soc.*, *63*, 187–216.

Rudnick, R. L., W. F. McDonough, and R. J. O'Connell (1998), Thermal structure, thickness and composition of continental lithosphere, *Chem. Geol.*, *145*, 395–411.

Ruppert, S., M. M. Fliedner, and G. Zandt (1998), Thin crust and active upper mantle beneath the southern Sierra Nevada in the western United States, *Tectonophysics*, *286*, 237–252.

Rychert, C. A., K. M. Fischer, and S. Rondenay (2005), A sharp lithosphere-asthenosphere boundary imaged beneath eastern North America, *Nature*, *436*, 542–545.

Saito, M. (1988), DISPER80: A subroutine package for the calculation of seismic normal-mode solutions, in *Seismological Algorithms*, edited by D. J. Doornbos, pp. 293–319, Elsevier, New York.

Saleeby, J., M. Ducea, and D. Clemens-Knott (2003), Production and loss of high-density batholithic root, southern Sierra Nevada, California, *Tectonics*, *22*(6), 1064, doi:10.1029/2002TC001374.

Savage, B., C. Ji, and D. V. Helmberger (2003), Velocity variations in the uppermost mantle beneath the southern Sierra Nevada and Walker Lane, *J. Geophys. Res.*, *108*(B7), 2325, doi:10.1029/2001JB001393.

Savage, M. K., and P. G. Silver (1993), Mantle deformation and tectonics: Constraints from seismic anisotropy in the western United States, *Phys. Earth Planet. Inter.*, *78*, 207–227.

Savage, M. K., L. Li, J. P. Eaton, C. H. Jones, and J. N. Brune (1994), Earthquake refraction profiles of the root of the Sierra Nevada, *Tectonics*, *13*, 803–817.

Schulte-Pelkum, V., G. Masters, and P. Shearer (2001), Upper mantle anisotropy from long-period P polarization, *J. Geophys. Res.*, *106*, 21,917–21,934.

Shapiro, N. M., M. Campillo, A. Paul, S. K. Singh, D. Jongmans, and F. J. Sanchez-Sesma (1997), Surface-wave propagation across the Mexican Volcanic Belt and the origin of the long-period seismic-wave amplification in the Valley of Mexico, *Geophys. J. Int.*, *128*, 151–166.

Sieminski, A., J.-J. Leveque, and E. Debayle (2004), Can finite-frequency effects be accounted for in ray theory surface wave tomography?, *Geophys. Res. Lett.*, *31*, L24614, doi:10.1029/2004GL021402.

Silver, L. T., and B. W. Chappell (1988), The Peninsular Ranges Batholith: An insight into the evolution of the Cordilleran batholiths of southwestern North America, *Trans. R. Soc. Edinburgh Earth Sci.*, *79*, 105–121.

Silver, P. G. (1996), Seismic anisotropy beneath the continents: Probing the depths of geology, *Annu. Rev. Earth Planet.*, *Sci.24*, 385–432.

Silver, P. G., and W. E. Holt (2002), The mantle flow field beneath western North America, *Science*, *295*, 1054–1057.

Smith, M. L., and F. A. Dahlen (1973), The azimuthal dependence of Love and Rayleigh wave propagation in a slightly anisotropic medium, *J. Geophys. Res.*, *78*, 3321–3333.

Stixrude, L., and C. Lithgow-Bertelloni (2005), Mineralogy and elasticity of the oceanic upper mantle: Origin of the low-velocity zone, *J. Geophys. Res.*, *110*, B03204, doi:10.1029/2004JB002965.

Tanimoto, T., and K. Prindle Sheldrake (2002), Three-dimensional S-wave velocity structure in Southern California, *Geophys. Res. Lett.*, *29*(8), 1223, doi:10.1029/2001GL013486.

Tarantola, A., and B. Valette (1982), Generalized non-linear problems solved using the least-squares criterion, *Rev. Geophys.*, *20*, 219–232.

van der Lee, S. (2002), High-resolution estimates of lithospheric thickness from Missouri to Massachusetts, USA, *Earth Planet. Sci. Lett.*, *203*, 15–23.

van Kooten, G. K. (1980), Mineralogy, petrology, and geochemistry of an ultra-potassic basaltic suite, central Sierra Nevada, California, USA, *J. Petrol.*, *21*, 651–684.

Walck, M. C., and J. B. Minster (1982), Relative array analysis of upper mantle lateral velocity variations in southern California, *J. Geophys. Res.*, *87*, 1754–1772.

Wang, J., and T. Teng (1994), Surface wave profiling of the lithosphere beneath the Mojave Desert using TERRAscope data, *J. Geophys. Res.*, *99*, 743–750.

Wang, K., T. Plank, J. D. Walker, and E. I. Smith (2002), A mantle melting profile across the Basin and Range, SW United States, *J. Geophys. Res.*, *107*(B1), 2017, doi:10.1029/2001JB000209.

Weeraratne, D. S., D. W. Forsyth, K. M. Fischer, and A. A. Nyblade (2003), Evidence for an upper mantle plume beneath the Tanzanian craton from Rayleigh wave tomography, *J. Geophys. Res.*, *108*(B9), 2427, doi:10.1029/2002JB002273.

Wernicke, B., et al. (1996), Origin of high mountains in the continents: The southern Sierra Nevada, *Science*, *271*, 190–193.

Wielandt, E. (1993), Propagation and structural interpretation of non-plane waves, *Geophys. J. Int.*, *113*, 45–53.

Yang, Y., and D. W. Forsyth (2006), Regional tomographic inversion of the amplitude and phase of Rayleigh waves with 2-D sensitivity kernels, *Geophys. J. Int.*, in press.

Zandt, G. (2003), The southern Sierra Nevada drip and the mantle wind direction beneath the southwestern United States, *Int. Geol. Rev.*, *45*, 213–224.

Zandt, G., and C. R. Carrigan (1993), Small-scale convective instability and upper mantle viscosity under California, *Science*, *261*, 460–463.

Zandt, G., H. Gilbert, T. J. Owens, M. Ducea, J. Saleeby, and C. H. Jones (2004), Active foundering of a continental arc root beneath the southern Sierra Nevada in California, *Nature*, *431*, 41–46.

Zhao, D., and H. Kanamori (1992), P-wave image of the crust and uppermost mantle in southern California, *Geophys. Res. Lett.*, *19*, 2329–2332.

Zhao, D., H. Kanamori, and E. Humphreys (1996), Simultaneous inversion of local and teleseismic data for the crust and mantle structure of southern California, *Phys. Earth Planet. Inter.*, *93*, 191–214.

Zhou, Y., F. A. Dahlen, and G. Nolet (2004), 3-D sensitivity kernels for surface-wave observables, *Geophys. J. Int.*, *158*, 142–168.

Zhu, L., and H. Kanamori (2000), Moho depth variation in southern California from teleseismic receiver functions, *J. Geophys. Res.*, *105*, 2969–2980.

---

D. W. Forsyth, Department of Geological Sciences, Brown University, Providence, RI 02912, USA.

Y. Yang, Center for Imaging the Earth's Interior, Department of Physics, University of Colorado, Boulder, CO 80309-0390, USA. (yingjie.yang@colorado.edu)